27

Emergence of Nonzonal Coherent Structures

NIKOLAOS A. BAKAS AND PETROS J. IOANNOU

27.1 INTRODUCTION

Atmospheric and oceanic turbulence is commonly observed to be organized into spatially and temporally coherent structures such as zonal jets and coherent vortices. A simple model that retains the relevant dynamics is a barotropic flow on a β-plane with turbulence sustained by random stirring. Numerical simulations of the stochastically forced barotropic vorticity equation on the surface of a rotating sphere or on a β-plane have shown the coexistence of robust zonal jets and of large-scale westward-propagating coherent structures that are referred to as satellite modes (Danilov and Gurarie, 2004) or zonons (Sukoriansky et al., 2008; Galperin et al., 2010). The emergence of these coherent structures in barotropic turbulence also has another feature. As the energy input of the stochastic forcing is increased or dissipation is decreased, there is a sudden onset of coherent zonal flows (Srinivasan and Young, 2012; Constantinou et al., 2014a) and nonzonal coherent structures (Bakas and Ioannou, 2013e). This argues that the emergence of coherent structures in a homogeneous background of turbulence is a bifurcation phenomenon.

An advantageous method to study such a phenomenon is to adopt the perspective of statistical state dynamics of the flow, rather than look into the dynamics of sample realizations of direct numerical simulations. This amounts to studying the dynamics and stability of the statistical equilibria arising in the turbulent flow, which are fixed points of the equations governing the evolution of the flow statistics. This approach is followed in the Stochastic Structural Stability Theory (S3T) (Farrell and Ioannou, 2003) or second-order cumulant expansion (CE2) (Marston et al., 2008). This theory is based on two building blocks. The first is to do a Reynolds decomposition of the dynamical variables into the sum of a mean value that represents the coherent flow and fluctuations that represent the turbulent eddies and then form the cumulants containing the information on the mean values (first cumulant) and on the eddy statistics (higher-order cumulants). The second building block is to truncate the equations governing the evolution of the cumulants at second order by either parameterizing the terms involving the third cumulant (Farrell and Ioannou, 1993a,b; DelSole and Farrell, 1996; DelSole, 2004b) or setting the third cumulant to zero (Marston et al., 2008; Tobias et al., 2011; Srinivasan and Young, 2012). Restriction of the dynamics to the first two cumulants is equivalent to neglecting the eddy–eddy interactions in the fully nonlinear dynamics and retaining only the interaction between the eddies and the instantaneous mean flow. While such a second-order closure might seem crude at first sight, there is strong evidence to support it (Bouchet et al., 2013).

Previous studies employing S3T have already addressed the bifurcation from a homogeneous turbulent regime to a jet-forming regime in barotropic β-plane turbulence and identified the emerging jet structures both numerically (Farrell and Ioannou, 2007) and analytically (Bakas and Ioannou, 2011; Srinivasan and Young, 2012) as linearly unstable modes to the homogeneous turbulent state equilibrium. It has also been shown that the resulting dynamical system for the evolution of the first two cumulants linearized around the homogeneous equilibrium possesses the mathematical structure of the dynamical system of pattern formation (Parker and Krommes, 2013). Comparison of the results of the stability analysis with direct numerical simulations have shown that the structure of zonal flows that emerge in the nonlinear simulations can be predicted by S3T (Srinivasan and Young, 2012; Constantinou et al., 2014a). However, these research efforts have assumed that the ensemble average employed in S3T is equivalent to a zonal average, a simplification that treats the nonzonal structures as incoherent and cannot address their emergence and effect on the jet dynamics. In addition, the eddy–mean flow dynamics underlying the S3T instability even in the jet formation case that involve only the interactions of small-scale waves with the large-scale coherent structures are not clear.

So, the goals in this chapter are the following. The first is to adopt a more general interpretation of the ensemble average, in order to address the emergence of coherent nonzonal structures. We adopt the more general interpretation that the ensemble average is a Reynolds average over the fast turbulent motions (Bernstein, 2009; Bernstein and Farrell, 2010). With this definition of the ensemble mean, we obtain the statistical dynamics of the interaction of the coarse-grained ensemble average field, which can be zonal or nonzonal coherent structures represented by their vorticity, with the fine-grained incoherent field represented by the vorticity second cumulant, and we revisit the structural stability of the homogeneous equilibrium under this assumption. The second goal is to study in detail the eddy–mean flow dynamics underlying the S3T instability, focusing on the example of jet formation. The third goal is to compare the characteristics of the structures that emerge in S3T against nonlinear simulations, even in highly nonlinear regimes that at first glance present a challenging test for the restricted nonlinear dynamics of S3T.

27.2 FORMULATION OF S3T UNDER A GENERALIZED AVERAGE

Consider a nondivergent barotropic flow on a β-plane with cartesian coordinates $\mathbf{x} = (x, y)$. The velocity field, $\mathbf{u} = (u, v)$, is given by $(u, v) = (-\partial_y \psi, \partial_x \psi)$, where ψ is the stream function. The relative vorticity $\zeta(x, y, t) = \Delta\psi$, evolves according to the nonlinear (NL) equation

$$(\partial_t + \mathbf{u} \cdot \nabla)\, \zeta + \beta v = -r\zeta - \nu\Delta^2 \zeta + f^{\mathrm{e}}, \tag{27.1}$$

where $\Delta = \partial^2_{xx} + \partial^2_{yy}$ is the horizontal Laplacian, β is the gradient of planetary vorticity, r is the coefficient of linear dissipation that typically parameterizes Ekman drag in planetary atmospheres and ν is the coefficient of hyperdiffusion that dissipates enstrophy flowing into unresolved scales. The exogenous forcing term f^{e}, parameterizes processes such as small-scale convection or baroclinic instability that are missing from the barotropic dynamics, and is necessary to sustain turbulence. We assume that f^{e} is a temporally delta-correlated and spatially homogeneous random stirring, injecting energy at a rate ε and having a two-point, two-time correlation function of the form

$$\left\langle f^{\mathrm{e}}(x_1, y_1, t_1) f^{\mathrm{e}}(x_2, y_2, t_2) \right\rangle = \delta(t_2 - t_1)\Xi(x_1, x_2, y_1, y_2), \tag{27.2}$$

where the brackets denote an ensemble average over the different realizations of the forcing.

S3T describes the statistical dynamics of the first two same-time cumulants of (27.1). The equations governing the evolution of the first two cumulants are obtained as follows. We decompose the vorticity field into the averaged field, $Z = \mathcal{T}[\zeta]$, defined as a time average over an intermediate timescale and deviations from the mean or eddies, $\zeta' = \zeta - Z$. The intermediate timescale is larger than the timescale of the turbulent motions but smaller than the timescale of the large-scale motions. With this decomposition, we rewrite (27.1) as

$$(\partial_t + \mathbf{U} \cdot \nabla)\, Z + \beta V = -\nabla \cdot \mathcal{T}[\mathbf{u}'\zeta'] - rZ - \nu\Delta^2 Z, \tag{27.3}$$

where $\mathbf{U} = [U, V] = [-\partial_y \Psi, \partial_x \Psi]$ and $\mathbf{u}' = [u', v'] = [-\partial_y \psi', \partial_x \psi']$ are the mean and the eddy velocity fields respectively. The mean vorticity is therefore forced by the divergence of the mean vorticity fluxes. The eddy vorticity ζ' evolves according to

$$\begin{aligned}(\partial_t + \mathbf{U} \cdot \nabla)\, \zeta' + (\beta + \partial_y Z) v' + u' \partial_x Z = \\ = -r\zeta' - \nu\Delta^2 \zeta' + f^{\mathrm{e}} + \underbrace{\mathcal{T}[\mathbf{u}' \cdot \nabla\zeta'] - \mathbf{u}' \cdot \nabla\zeta'}_{f^{\mathrm{NL}}},\end{aligned} \tag{27.4}$$

where f^{NL} is the term involving the nonlinear interactions among the turbulent eddies. A closed system for the statistical state dynamics is obtained by first neglecting the eddy–eddy term f^{NL} to obtain the quasi-linear system:

$$(\partial_t + \mathbf{U} \cdot \nabla)\, Z + \beta V = -\nabla \cdot \mathcal{T}[\mathbf{u}'\zeta'] - rZ - \nu\Delta^2 Z, \tag{27.5}$$

$$(\partial_t + \mathbf{U} \cdot \nabla)\, \zeta' + (\beta + \partial_y Z) v' + u' \partial_x Z = -r\zeta' - \nu\Delta^2 \zeta' + f^{\mathrm{e}}. \tag{27.6}$$

In order to obtain the statistical dynamics of the quasi-linear system of (27.5) and (27.6) we adopt the general interpretation that the ensemble average over the forcing realizations is equal to the time average over the intermediate timescale (Bernstein, 2009; Bernstein and Farrell, 2010). Under this assumption, the slowly varying mean flow Z is also the first cumulant of the vorticity $Z = \langle\zeta\rangle$, where the brackets denote the ensemble average. The time mean of the vorticity flux is equal to the ensemble mean of the flux, $\mathcal{T}[\mathbf{u}'\zeta'] = \langle\mathbf{u}'\zeta'\rangle$. The fluxes can be related to the second cumulant $C(\mathbf{x}_1, \mathbf{x}_2, t) \equiv \langle\zeta'(\mathbf{x}_1)\zeta'(\mathbf{x}_2)\rangle$, which is the correlation function of the eddy vorticity between the two points $\mathbf{x}_i = (x_i, y_i)$, $i = 1, 2$. We hereafter indicate the dynamic variables that are functions of points $\mathbf{x}_i$ with the subscript i, that is, $\zeta'_i \equiv \zeta'(\mathbf{x}_i)$. By making the identification that the fluxes at point $\mathbf{x}$ are equal to the value of the two-variable function $\left\langle \mathbf{u}'_1 \zeta'_2 \right\rangle$ evaluated at the same point $\mathbf{x} = \mathbf{x}_1 = \mathbf{x}_2$, we write the fluxes as

$$\langle \mathbf{u}'\zeta' \rangle = \left\langle \mathbf{u}'_1 \zeta'_2 \right\rangle_{\mathbf{x}_1 = \mathbf{x}_2}. \tag{27.7}$$

Expressing the velocities in terms of the vorticity $[u', v'] = [-\partial_y \Delta^{-1}, \partial_x \Delta^{-1}]\zeta'$, where Δ^{-1} is the integral operator that inverts vorticity into the stream function field, we obtain the vorticity fluxes as a function of the second cumulant in the following manner:

$$\begin{aligned}\langle \mathbf{u}'\zeta' \rangle &= \left[\left\langle u'_1 \zeta'_2 \right\rangle_{\mathbf{x}_1 = \mathbf{x}_2}, \left\langle v'_1 \zeta'_2 \right\rangle_{\mathbf{x}_1 = \mathbf{x}_2} \right] \\ &= \left[-\left\langle \partial_{y_1} \Delta_1^{-1} \zeta'_1 \zeta'_2 \right\rangle_{\mathbf{x}_1 = \mathbf{x}_2}, \left\langle \partial_{x_1} \Delta_1^{-1} \zeta'_1 \zeta'_2 \right\rangle_{\mathbf{x}_1 = \mathbf{x}_2} \right] \\ &= \left[-\left(\partial_{y_1} \Delta_1^{-1} C \right)_{\mathbf{x}_1 = \mathbf{x}_2}, \left(\partial_{x_1} \Delta_1^{-1} C \right)_{\mathbf{x}_1 = \mathbf{x}_2} \right].\end{aligned} \tag{27.8}$$

Consequently, the first cumulant evolves according to

$$\begin{aligned}\partial_t Z + U Z_x + V(\beta + Z_y) + rZ + \nu\Delta^2 Z = \\ = \partial_x \left(\partial_{y_1} \Delta_1^{-1} C \right)_{\mathbf{x}_1 = \mathbf{x}_2} - \partial_y \left(\partial_{x_1} \Delta_1^{-1} C \right)_{\mathbf{x}_1 = \mathbf{x}_2}.\end{aligned} \tag{27.9}$$

Multiplying (~~27.A.5~~) for $\partial_t \zeta'_1$ by ζ'_2 and (~~27.A.5~~) for $\partial_t \zeta'_2$ by ζ'_1, adding the two equations and taking the ensemble average yields the equation for the second cumulant C:

$$\partial_t C - (A_1 + A_2) C = \left\langle f^{\mathrm{e}}_1 \zeta'_2 + f^{\mathrm{e}}_2 \zeta'_1 \right\rangle, \tag{27.10}$$

where

$$A_i = -\mathbf{U}_i \cdot \nabla_i - (\beta + \partial_{y_i} Z)\partial_{x_i} \Delta_i^{-1} + \partial_{x_i} Z \partial_{y_i} \Delta_i^{-1} - r - \nu\Delta_i^2 \tag{27.11}$$

governs the dynamics of linear perturbations about the instantaneous mean flow $\mathbf{U}$. The right-hand side of (27.10) is the correlation of the external forcing with vorticity, which for delta-correlated stochastic forcing is independent of the state of the flow and is equal at all times to the prescribed forcing covariance: $\left\langle f^{\mathrm{e}}_1 \zeta'_2 + f^{\mathrm{e}}_2 \zeta'_1 \right\rangle = \left\langle f^{\mathrm{e}}_1 f^{\mathrm{e}}_2 \right\rangle = \Xi$. Therefore, the second cumulant evolves according to

$$\partial_t C = (A_1 + A_2) C + \Xi, \tag{27.12}$$

and forms with (27.9) the closed autonomous system of S3T theory that determines the statistical dynamics of the flow approximated at second order.

The S3T system has bounded solutions (see Appendix 27.A) and the fixed points Z^{E} and C^{E}, if they exist, define statistical equilibria of the coherent structures with vorticity Z^{E} in the presence of an eddy field with second-order cumulant or covariance C^{E}. The structural stability of these statistical equilibria addresses the parameters in the physical system that

can lead to abrupt reorganization of the turbulent flow. Specifically, when an equilibrium of the S3T equations becomes unstable as a physical parameter changes, the turbulent flow bifurcates to a different attractor. In this work, we show that coherent structures emerge as unstable modes of the S3T system and equilibrate at finite amplitude. The predictions of S3T regarding the emergence and characteristics of the coherent structures are then compared to the nonlinear simulations of the stochastically forced barotropic flow.

27.3 S3T INSTABILITY AND EMERGENCE OF FINITE-AMPLITUDE LARGE-SCALE STRUCTURE

The homogeneous equilibrium with no mean flow,

$$Z^{\mathrm{E}} = 0, \quad C^{\mathrm{E}} = \frac{\Xi}{2r}, \tag{27.13}$$

is a fixed point of the S3T system (27.9) and (27.12) in the absence of hyperdiffusion (see Appendix 27.B). The linear stability of the homogeneous equilibrium can be addressed by performing an eigenanalysis of the S3T system linearized about this equilibrium. The eigenfunctions in this case have the plane-wave form

$$\delta Z = Z_{nm} e^{\mathbf{n}\cdot\mathbf{x}} e^{\sigma t}, \quad \delta C = C_{nm}(\tilde{\mathbf{x}}) e^{i\mathbf{n}\cdot\bar{\mathbf{x}}} e^{\sigma t}, \tag{27.14}$$

where $\tilde{\mathbf{x}} = \mathbf{x}_1 - \mathbf{x}_2$, $\bar{\mathbf{x}} = (\mathbf{x}_1 + \mathbf{x}_2)/2$, $\mathbf{n} = (n, m)$ is the wavevector of the eigenfunction and $\sigma = \sigma_{\mathrm{r}} + i\sigma_{\mathrm{i}}$ is the eigenvalue with $\sigma_{\mathrm{r}} = \mathrm{Re}(\sigma)$, $\sigma_{\mathrm{i}} = \mathrm{Im}(\sigma)$ being the growth rate and frequency of the mode, respectively. The eigenvalue σ satisfies the nondimensional equation

$$\begin{aligned}\frac{\tilde{\varepsilon}}{2\pi r^3 L_{\mathrm{f}}^2} \int_{-\infty}^{\infty}\int_{-\infty}^{\infty} \mathrm{d}\tilde{k}\mathrm{d}\tilde{l}(1-\tilde{N}^2/\tilde{K}^2)\hat{\Xi}(\tilde{k},\tilde{l})\times \\ \times \frac{(\tilde{m}\tilde{k}-\tilde{n}\tilde{l})\left[\tilde{n}\tilde{m}(\tilde{k}_+^2-\tilde{l}_+^2)+(\tilde{m}^2-\tilde{n}^2)\tilde{k}_+\tilde{l}_+\right]}{i\tilde{\beta}\left(\tilde{k}\tilde{K}_s^2-(\tilde{k}+\tilde{n})\tilde{K}^2\right)+(\tilde{\sigma}+2)\tilde{K}^2\tilde{K}_s^2} = \\ = (\tilde{\sigma}+1)\tilde{N}^2 - i\tilde{n}\tilde{\beta},\end{aligned} \tag{27.15}$$

where L_{f} is a characteristic length scale, $\tilde{\sigma} = \sigma/r$ and $(\tilde{n}, \tilde{m}) = L_{\mathrm{f}}(n, m)$ are the nondimensional eigenvalue and wavenumbers respectively, $\tilde{\varepsilon} = \varepsilon/(r^3 L_{\mathrm{f}}^2)$ is the nondimensional energy injection rate of the forcing, $\tilde{\beta} = \beta L_{\mathrm{f}}/r$ is the nondimensional planetary vorticity gradient,

$$\hat{\Xi}(k,l) = \frac{1}{2\pi}\int_{-\infty}^{\infty}\int_{-\infty}^{\infty} \Xi(\tilde{x},\tilde{y}) e^{-ik\tilde{x}-il\tilde{y}}\mathrm{d}\tilde{x}\mathrm{d}\tilde{y} \tag{27.16}$$

is the Fourier transform of the forcing covariance, $\tilde{K}^2 = \tilde{k}^2 + \tilde{l}^2$, $\tilde{K}_s^2 = (\tilde{k}+\tilde{n})^2 + (\tilde{l}+\tilde{m})^2$, $\tilde{N}^2 = \tilde{n}^2 + \tilde{m}^2$, $\tilde{k}_+ = \tilde{k} + \tilde{n}/2$ and $\tilde{l}_+ = \tilde{l} + \tilde{m}/2$ (see Appendix 27.B). For a forcing with the mirror symmetry $\hat{\Xi}(k,-l) = \hat{\Xi}(k,l)$ in wavenumber space and for $\tilde{n} \neq 0$, the eigenvalues satisfy the relations:

$$\tilde{\sigma}_{(-\tilde{n},\tilde{m})} = \tilde{\sigma}^*_{(\tilde{n}\tilde{m})}, \text{ and } \tilde{\sigma}_{(\tilde{n},-\tilde{m})} = \tilde{\sigma}_{(\tilde{n},\tilde{m})}, \tag{27.17}$$

implying that the growth rates depend on $|\tilde{n}|$ and $|\tilde{m}|$. As a result, the plane wave $\delta Z = \cos(nx + my)$ and an array of localized vortices $\delta Z = \cos(nx)\cos(my)$ have the same growth rate, despite their different structure. For zonally symmetric perturbations with $\tilde{n} = 0$, only the second relation in (27.17) holds and (27.15) reduces to the stability equation derived by Srinivasan and Young (2012) for the emergence of jets in a barotropic β-plane.

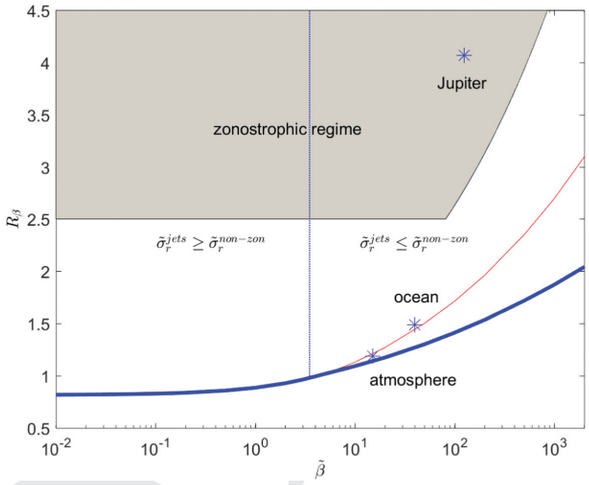

Figure 27.1 The critical zonostrophy parameter $R_\beta = 0.7(\tilde{\varepsilon}_{\mathrm{c}}\tilde{\beta}^2)^{1/20}$ for structural instability (thick line) and the corresponding critical parameter for structural instability of zonal jets (thin line) as a function of $\tilde{\beta}$. The shaded region denotes the zonostrophic regime for which both the inequalities $R_\beta \geq 2.5$ and $k_\beta/K_{\mathrm{f}} \leq 1/4$ are satisfied. The thin dotted vertical line $\tilde{\beta} = \tilde{\beta}_{\min}$ separates the unstable region: for $\tilde{\beta} < \tilde{\beta}_{\min}$ zonal structures grow the most, whereas for $\tilde{\beta} > \tilde{\beta}_{\min}$ nonzonal structures grow the most. The stars denote the position of the Earth's atmosphere and ocean as well as the Jovian atmosphere in the $R_\beta, \tilde{\beta}$ parameter space.

We consider the case of a ring forcing that injects energy at rate ε at the total wavenumber K_{f}:

$$\hat{\Xi}(k,l) = 2\varepsilon K_{\mathrm{f}}\delta(\sqrt{k^2+l^2} - K_{\mathrm{f}}), \tag{27.18}$$

and obtain the eigenvalues $\tilde{\sigma}$ by numerically solving (27.15).[1] For small values of the energy input rate, $\tilde{\sigma}_{\mathrm{r}} < 0$ for all wavenumbers and the homogeneous equilibrium is stable. At a critical $\tilde{\varepsilon}_{\mathrm{c}}$ the homogeneous flow becomes S3T unstable and exponentially growing coherent structures emerge. The critical value, $\tilde{\varepsilon}_{\mathrm{c}}$, is calculated by first determining the energy input rate $\tilde{\varepsilon}_t(\tilde{n}, \tilde{m})$ that renders wavenumbers $(\tilde{n}, \tilde{m})$ neutral $(\tilde{\sigma}_{\mathrm{r}(\tilde{n},\tilde{m})} = 0)$, and then by finding the minimum energy input rate over all wavenumbers: $\tilde{\varepsilon}_{\mathrm{c}} = \min_{(\tilde{n},\tilde{m})}\tilde{\varepsilon}_t$. In Fig. 27.1 we show the corresponding critical zonostrophy parameter $R_\beta = 0.7(\tilde{\varepsilon}_{\mathrm{c}}\tilde{\beta}^2)^{1/20}$ which was used in previous studies to characterize the emergence and structure of zonal jets in planetary turbulence (Galperin et al., 2010), as a function of $\tilde{\beta}$. The absolute minimum energy input rate required is $\tilde{\varepsilon}_{\mathrm{c}} = 67$ and occurs at $\tilde{\beta}_{\min} = 3.5$, while the minimum zonostrophy parameter required for the emergence of coherent flows is $R_\beta^{\min} = 0.82$ and occurs for $\tilde{\beta} \to 0$. The asymptotic approach towards $R_\beta^{\min}$ as $\beta \to 0$ means that the critical input rate increases as $\tilde{\varepsilon}_{\mathrm{c}} \sim \tilde{\beta}^{-2}$ for $\tilde{\beta} \to 0$ and therefore the homogeneous equilibrium is structurally stable for all excitation amplitudes when $\tilde{\beta} = 0$. How-

[1] The characteristic length scale in this case is taken to be the length scale of the forcing, $L_{\mathrm{f}} = 1/K_{\mathrm{f}}$.

ever, the structural stability for $\tilde{\beta} = 0$ is an artifact of the assumed isotropy of the excitation and the assumption of a barotropic flow. In the presence of even the slightest anisotropy (Bakas and Ioannou, 2011, 2013b), or in the case of a stratified flow (see Chapter 26), zonal jets are S3T unstable and are expected to emerge even in the absence of β. For $\tilde{\beta} \leq \tilde{\beta}_{\min}$, the structures that first become marginally stable are zonal jets (with $n = 0$), while for $\tilde{\beta} > \tilde{\beta}_{\min}$ the marginally stable structures are nonzonal and the critical R_β grows as $R_\beta \sim \tilde{\beta}^{1/8}$ for $\tilde{\beta} \to \infty$. Since the critical R_β for the emergence of zonal jets (also shown in Fig. 27.1), increases as $R_\beta \sim \tilde{\beta}^{1/4}$ for $\tilde{\beta} \to \infty$, for large values of $\tilde{\beta}$ nonzonal structures first emerge and only at significantly higher $\tilde{\varepsilon}$ are zonal jets expected to appear. Investigation of these results with other forcing distributions revealed that the results for $\tilde{\beta} \gg 1$ are independent of the structure of the forcing (Bakas et al., 2015).

The parameter regime of S3T instability is now related to the results of previous studies and to geophysical flows. Previous studies have identified a parameter regime which is distinguished by robust, slowly varying zonal jets as well as propagating, nondispersive, nonzonal coherent structures (Galperin et al., 2010). This regime, termed zonostrophic, is in a region in parameter space in which the zonostrophy parameter is large ($R_\beta \geq 2.5$) and the scale $k_\beta = 0.5(\beta^3/\varepsilon)^{1/5}$ in which anisotropization of the turbulent spectrum occurs is sufficiently larger than the forcing scale ($k_\beta/K_f \leq 1/4$). This regime is shown in Fig. 27.1 to be highly supercritical for all $\tilde{\beta}$. In addition, Bakas and Ioannou (2013c) calculated indicative order-of-magnitude values of $\tilde{\beta}$ and $\tilde{\varepsilon}$ for the Earth's atmosphere and ocean as well as for the Jovian atmosphere. From these values we calculated the relevant zonostrophy parameter R_β and indicated the three geophysical flows in Fig. 27.1. We can see that all three cases are supercritical: the Jovian atmosphere is highly supercritical and is well within the zonostrophic regime, while the Earth's atmosphere and ocean are slightly supercritical (at least within the context of the simplified barotropic model).

We now examine the growth rate and dispersion properties of the unstable modes for $\tilde{\varepsilon} > \tilde{\varepsilon}_c$ and consider first the case $\tilde{\beta} = 1$, with $\tilde{\varepsilon} = 2\tilde{\varepsilon}_c$. The growth rate of the maximally growing eigenvalue, $\tilde{\sigma}_r$, and its associated frequency of the mode, $\tilde{\sigma}_i$, are plotted in Fig. 27.2(a) as a function of $|\tilde{n}|$ and $|\tilde{m}|$. We observe that the region in wavenumber space defined roughly by $0 < |\tilde{n}| < 1/2$ and $1/2 < |\tilde{m}| < 1$ is unstable, with the maximum growth rate occurring for zonal structures ($\tilde{n} = 0$) with $|\tilde{m}| \simeq 0.8$. The frequency of the unstable modes is zero for zonal jet perturbations ($\tilde{n} = 0$) and non-negative for all other wavenumbers ($\tilde{n} \neq 0$). Using the symmetries (27.17), this implies that unstable mean flow perturbations δZ propagate in the retrograde direction if $\tilde{n} \neq 0$ and are stationary when $\tilde{n} = 0$. As $\tilde{\varepsilon}$ increases the instability region expands and roughly covers the sector $1/2 < |\tilde{N}| < 1$, with zonal structures having a larger growth rate compared to nonzonal structures, a result that holds for any $\tilde{\varepsilon}$ when $\tilde{\beta} < \tilde{\beta}_{\min}$.

For $\tilde{\beta} > \tilde{\beta}_{\min}$ the nonzonal structures always have larger growth rate. This is illustrated in Fig. 27.2(b), showing the growth rates and frequencies of the unstable modes for $\tilde{\beta} = 10$. For larger $\tilde{\beta}$ values there is a tendency for the frequency of the unstable modes to conform to the corresponding Rossby wave

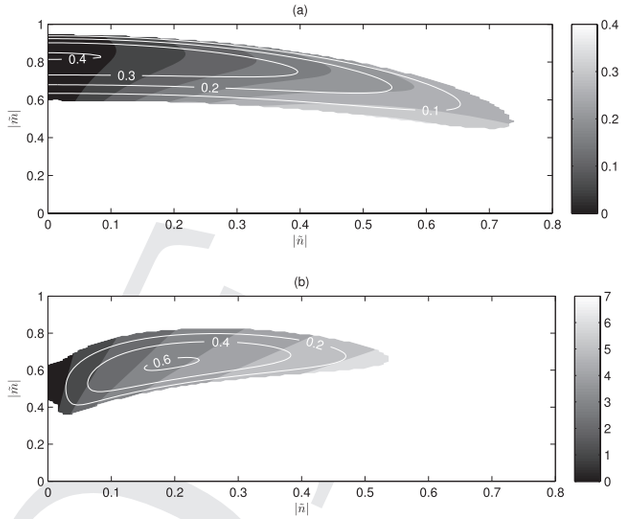

Figure 27.2 Dispersion relation of the unstable modes for $\tilde{\beta} = 1$ (a) and $\tilde{\beta} = 10$ (b). The contours show the growth rate $\tilde{\sigma}_r$ and the shading shows the frequency $\tilde{\sigma}_i$ of the unstable modes. For $\tilde{\beta}$ $O(1)$ stationary zonal jets are more unstable, and for $\tilde{\beta} \gg 1$ westward-propagating nonzonal structures are more unstable. For both panels, the energy input rate is $\tilde{\varepsilon} = 2\tilde{\varepsilon}_c$. Adapted from Bakas and Ioannou (2013c). © Cambridge University Press. Reprinted with permission.

frequency

$$\tilde{\sigma}_R = \frac{\tilde{\beta}\tilde{n}}{\tilde{n}^2 + \tilde{m}^2}, \tag{27.19}$$

a tendency that does not occur for smaller $\tilde{\beta}$. A comparison between the frequency of the unstable modes and the Rossby wave frequency is shown in Fig. 27.3 in a plot of $\tilde{\sigma}_i/\tilde{\sigma}_R$. For slightly supercritical $\tilde{\varepsilon}$ the ratio is close to one and the unstable modes satisfy the Rossby wave dispersion relation. At higher supercriticalities, though, $\tilde{\sigma}_i$ departs from the Rossby wave frequency – by as much as 40% for the case of $\tilde{\varepsilon} = 50\tilde{\varepsilon}_c$ shown in Fig. 27.3(b).

27.4 ANALYSIS OF THE EDDY–MEAN FLOW DYNAMICS UNDERLYING JET FORMATION

It is interesting to investigate the eddy–mean flow dynamics underlying the structure-forming S3T instability. These dynamics should have the property of directly channeling energy from the turbulent motions to the coherent flow without the presence of a turbulent cascade. The dynamics underlying the formation of nonzonal structures were investigated by Bakas et al. (2015), who showed that for $\tilde{\beta} \gg 1$ the nonzonal structures emerge due to resonant and near-resonant interactions of the nonzonal structure with wavenumber $\mathbf{n}$ with a stochastically forced eddy with wavenumber $\mathbf{k}$ satisfying the resonant condition $\omega_{\mathbf{n}+\mathbf{k}} = \omega_{\mathbf{n}} + \omega_{\mathbf{k}}$ with ω the Rossby wave frequency. In the case of a monochromatic deterministic forcing, this mechanism is referred to as modulational instability (Connaughton et al., 2010b) and, as shown by Bakas et al. (2015) and Chapter 26 of this volume, the S3T instability is a generalization

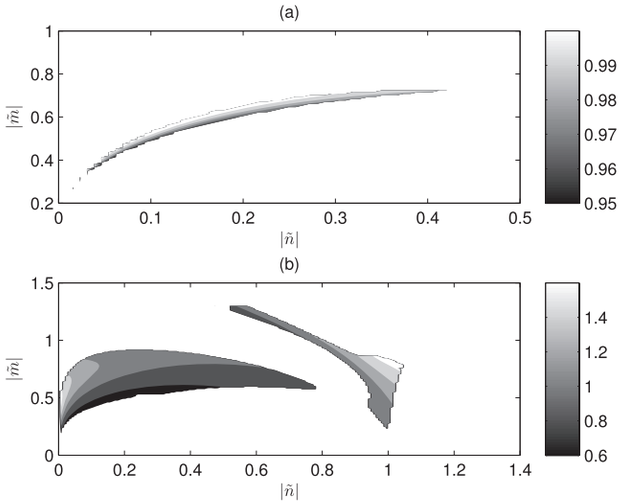

Figure 27.3 Ratio of the frequency of the unstable modes $\tilde{\sigma}_{\rm i}$ over the corresponding frequency of a Rossby wave with the same wavenumbers $\tilde{\sigma}_{\rm R}$ at (a) $\tilde{\varepsilon} = 2\tilde{\varepsilon}_{\rm c}$ and (b) $\tilde{\varepsilon} = 50\tilde{\varepsilon}_{\rm c}$ when $\tilde{\beta} = 100$. Values of 1 denote an exact match with the Rossby wave frequency. Adapted from Bakas and Ioannou (2013c). © Cambridge University Press. Reprinted with permission.

of modulational instability in a stochastic framework. In this section we focus on the dynamics underlying zonal jet formation that were also shown by Bakas et al. (2015) to govern the emergence of nonzonal structures when $\tilde{\beta} = O(1)$ and $\tilde{\beta} \ll 1$.

Previous studies have identified such mechanisms for the maintenance of zonal jets. Huang and Robinson (1998) showed that shear straining of the turbulent field by the jet produced up-gradient momentum fluxes that maintained the jet against dissipation. A simple case that clearly illustrates the physical picture for the mechanism of shear straining is to consider the evolution of eddies in a planar, inviscid constant-shear flow. The eddies are sheared by the mean flow into thinner elliptical shapes, while their vorticity is conserved. For an elongated eddy this implies that the eddy velocities decrease and the eddy energy is transferred to the mean flow through up-gradient momentum fluxes. This mechanism can operate when the time required for the eddies to shear over is much shorter than the dissipation timescale. The reason is that in this limit even the eddies with stream function leaning against the shear, which initially widen significantly and gain momentum, have the necessary time to shear over, elongate and surrender their momentum to the mean flow. Given that for an emerging jet the characteristic shear timescale is necessarily infinitely longer than the dissipation timescale, it needs to be shown that shear straining can produce up-gradient momentum fluxes in this case as well. In addition, previous studies have shown that shearing of isotropic eddies on an infinite domain does not produce any net momentum fluxes (Shepherd, 1985; Farrell, 1987; Holloway, 2010) and should have no effect on the S3T instability (Srinivasan and Young, 2012). Therefore, another mechanism should be responsible for producing the up-gradient fluxes in the case of an isotropic forcing.

In order to investigate the eddy–mean flow dynamics underlying the S3T instability, we calculate the vorticity flux divergence that is induced when the statistical equilibrium (27.13) is perturbed by an infinitesimal coherent structure δZ. For an S3T unstable structure, the induced flux divergence tends to enhance the coherent structure δZ, producing the positive feedback required for instability. So the goal of this section is to illuminate the eddy–mean flow dynamics leading to this positive feedback and to understand qualitatively why the homogeneous equilibrium is more stable for small and large values of $\tilde{\beta}$.

For zonal mean flows, (27.9) and (27.12) are respectively simplified to

$$\partial_t U = -\partial_y \langle u'v' \rangle - rU = \partial_y \left(\partial^2_{y_2 x_1} \Delta_1^{-1} C \right)_{\mathbf{x}_1 = \mathbf{x}_2} - rU \tag{27.20}$$

and

$$\partial_t C = (A_1 + A_2)C + \Xi, \tag{27.21}$$

where

$$A_i = -U_i \partial_{x_i} - (\beta - \partial^2_{y_i y_i} U)\Delta_i^{-1} \partial_{x_i} - r, \tag{27.22}$$

As a result, the zonal mean flow is driven by the momentum flux divergence of the eddies. The perturbation in vorticity covariance δC that is induced by the mean flow perturbation δU can be estimated immediately by assuming that the system (27.20)–(27.21) is very close to the stability boundary, so that the growth rate is small. In this case the mean flow evolves slowly enough that it remains in equilibrium with the eddy covariance, that is, $d\delta C/dt \simeq 0$. Bakas and Ioannou (2013b) showed that the ensemble mean momentum flux induced by an infinitesimal sinusoidal mean flow perturbation $\delta U = \epsilon \sin(my)$, where $\epsilon \ll 1$ – i.e. the eigenfunction of (27.B.4) – is equal in this case to the integral over time and over all zonal wavenumbers of the responses to all point excitations in the y direction:

$$\delta \langle u'v' \rangle = \frac{1}{2\pi} \int_{-\infty}^{\infty} \int_{-\infty}^{\infty} \int_{0}^{\infty} \overline{u'v'}(t) \mathrm{d}t \mathrm{d}\xi \mathrm{d}k, \tag{27.23}$$

where $\overline{u'v'}(t)$ is the momentum flux at time t produced by

$$G(k, y - \xi) = B(k) h(y - \xi) e^{ikx + il_0(y-\xi)}. \tag{27.24}$$

The Green's function G has the form of a wavepacket with an amplitude $B(k)$ and a carrier wave with wavenumbers (k, l_0) that is modulated in the y direction by the wavepacket envelope $h(y)$. The characteristics of the amplitude, the wavenumber and the envelope depend on the forcing characteristics, but in any case the calculation of the ensemble mean momentum fluxes is reduced to calculating the momentum fluxes $\overline{u'v'}(t)$ over the life cycle of wavepackets that are initially at different latitudes ξ and then adding their relative contributions.

As the wavepacket propagates in the latitudinal direction, its meridional wavenumber and frequency change due to shearing by the mean flow and due to the change of the mean vorticity gradient $\beta - U_{yy}$. The resulting time-variable momentum flux $\overline{u'v'}(t)$ can be calculated using ray tracing. According to standard ray-tracing arguments, the wave action is conserved along a ray (in the absence of dissipation), leading to the momentum flux

$$\overline{u'v'}(t) = -|B|^2 A_{\rm M}(t) e^{-2rt} |h(y - \eta(t))|^2, \tag{27.25}$$

where $A_M(t) = kl_t/(k^2 + l_t^2)^2$ is the momentum flux of the carrier wave that determines the amplitude of the fluxes of the wavepacket and l_t, $\eta(t)$ are the time-dependent meridional wavenumber and position of the wavepacket, respectively (Andrews et al., 1987). Because of the small amplitude of the mean flow perturbation δU, the wavenumber and position of the packet vary slowly on a timescale $O(\epsilon t)$ compared to the dissipation timescale $1/r$, and the dominant contribution to the time integral in (27.23) comes from small times. We can therefore seek asymptotic solutions of the form

$$l_t = l_0 + \epsilon l_1(t) + \cdots, \quad \eta(t) = \xi + c_0 t + \epsilon\eta_1(t) + \cdots, \tag{27.26}$$

where $c_0 = 2\beta k l_0/(k^2+l_0^2)^2$ is the group velocity in the absence of a mean flow, and calculate the integral of $\overline{u'v'}(t)$ over time from the leading-order terms. Substituting (27.26) in (27.25), we obtain

$$\begin{aligned}\overline{u'v'}(t) = &\underbrace{-|B|^2 A_M(0) e^{-2rt}|h(y-\xi-c_0t)|^2}_{\overline{u'v'}_R} - \\ &\underbrace{-\epsilon|B|^2\left(\frac{dA_M}{dl_t}\right)_{l_0} l_1(t) e^{-2rt}|h(y-\xi-c_0t)|^2}_{\overline{u'v'}_S} \\ &\underbrace{-\epsilon|B|^2 A_M(0)\eta_1(t) e^{-2rt}\frac{d}{dy}|h(y-\xi-c_0t)|^2}_{\overline{u'v'}_\beta}.\end{aligned} \tag{27.27}$$

The first term, $\overline{u'v'}_R$, arises from the momentum flux produced by a wavepacket in the absence of a mean flow. Because $A_M(0) = kl_0/(k^2+l_0^2)^2$ is odd with respect to wavenumbers, this term does not contribute to the ensemble-averaged momentum flux when integrated over all wavenumbers and will hereafter be ignored. The second term, $\overline{u'v'}_S$, arises from the small change in the amplitude of the flux A_M over a dissipation timescale. The third term, $\overline{u'v'}_\beta$, arises from the small change in the position of the packet η compared to a propagating packet in the absence of a mean flow. To summarize, the infinitesimal mean flow refracts the wavepacket due to shearing and due to the change of the mean vorticity gradient, and slightly changes the amplitude of the fluxes as well as slightly ~~speeding~~ up or ~~slowing~~ down the wavepacket. The sum of these two effects will produce the induced momentum fluxes.

27.4.1 The Limit of Small-Scale Wavepackets with a Short Propagation Range

In order to clearly illustrate the behavior of the eddy fluxes, we consider the limit of $\tilde{\beta} = \beta L_f/r \ll 1$, where L_f is the scale of the wavepackets, and in addition we assume that the scale of the mean flow, $1/m$, is much larger than the scale of the wavepackets $mL_f \ll 1$. In this limit, the wavepackets are dissipated before propagating far from the initial position, and the effect of the change in the mean vorticity gradient is higher order. As a result, Bakas and Ioannou (2013b) showed that l_1 and η_1 decrease monotonically with time with rates independent of δU_{yy} and proportional to the shear $\delta U_y(\xi)$ at the initial position ξ:

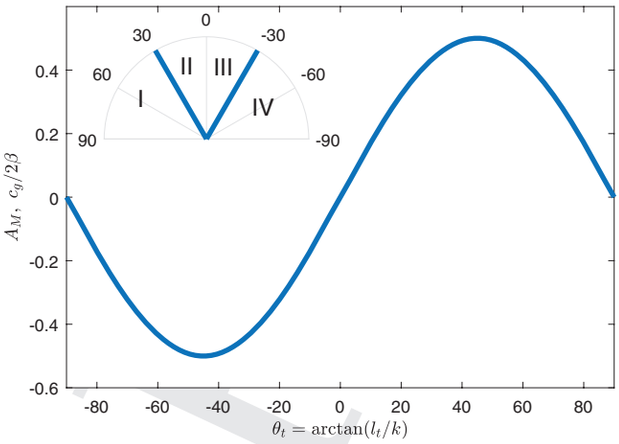

Figure 27.4 Amplitude of the momentum fluxes, $A_M(t)$, of wavepackets as a function of the angle $\theta_t = \arctan(l_t/k)$ between the phase lines of the central wave and the y-axis. The inset shows the possible phase line orientations $\theta_t = \arctan(l_t/k)$ in a polar plot and the regions with $|\theta_t| < \pi/6$ (II and III) and $|\theta_t| > \pi/6$ (I and IV).

$$l_1(t) = -\delta U_y(\xi)kt, \quad \eta_1(t) = -\beta\delta U_y(\xi)\left(\frac{dA_M}{dl_t}\right)_{l_0} kt^2. \tag{27.28}$$

That is, the amplitude of the flux A_M and the group velocity of the packets change only due to the shearing of the carrier wave by the local shear.

Consider in this limit the first term, $\overline{u'v'}_S$, arising from the small amplitude change. For $\tilde{\beta} \ll 1$ the wavepacket is dissipated before it propagates away and we can ignore to first-order propagation:

$$\begin{aligned}\overline{u'v'}_S &= -\epsilon|B|^2\left(\frac{dA_M}{dl_t}\right)_{l_0} l_1(t) e^{-2rt}|h(y-\xi-c_0t)|^2 \\ &\simeq |B|^2\delta U_y(\xi)kt\left(\frac{dA_M}{dl_t}\right)_{l_0} e^{-2rt}|h(y-\xi)|^2,\end{aligned} \tag{27.29}$$

so that the packet grows/decays in situ. Since the wave packet is rapidly dissipated, the integrated momentum flux over its lifetime will be given to a good approximation by the instantaneous change in the flux[2] that is proportional to $(dA_M/dl_t)_{l_0}$. Figure 27.4 illustrates the amplitude of the momentum flux as a function of the angle $\theta_t = \arctan(l_t/k)$ of the phase lines of the carrier wave of the packet with the y-axis. It is shown that the derivative of A_M of a wavepacket with $|\theta_0| < \pi/6$ (that is, with phase lines close to the meridional direction) excited in regions II or III is positive. This leads to increased fluxes compared to an unsheared wavepacket, as shown in Fig. 27.5(a), and to up-gradient momentum flux as shown in Fig. 27.6(a). The opposite occurs for waves excited in regions I and IV (with $|\theta_0| > \pi/6$) that produce down-gradient flux, as their momentum flux decreases.

We now consider the second term, $\overline{u'v'}_\beta$, arising from the effect of propagation on the momentum flux. The group velocity of the wavepacket is given by $c_g = 2\beta A_M$, shown in Fig. 27.4

[2] The change in flux occurs over the dissipation timescale $1/r$, which is incremental in shear time units.

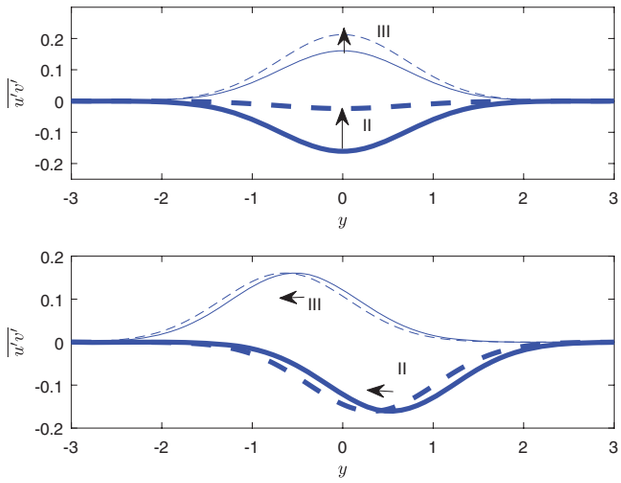

Figure 27.5 (a) Comparison of the momentum fluxes of an unsheared wavepacket excited in regions II (thick solid line) and III (solid line) to the momentum fluxes of a sheared wavepacket shown by the corresponding dashed lines, when only the change in amplitude is taken into account. A snapshot of the fluxes at $t = 0.25/r$ is shown. The arrows show the increase in the fluxes. The wavenumber is $\sqrt{k^2 + l_0^2} = 1$, $h(y) = e^{-y^2/2}$, $|\theta_0| = 16°$, $|B| = 1$ and the shear $\delta U_y = r$ for illustration purposes. (b) Comparison of the momentum fluxes of an unsheared wavepacket excited in regions II (thick solid line) and III (solid line) to the momentum fluxes of a sheared wavepacket shown by the corresponding dashed lines, when only the change in propagation is taken into account. The arrows show the change in position compared to an unsheared packet. $\beta = 4$ for illustration purposes, and the rest of the parameters are as in (a).

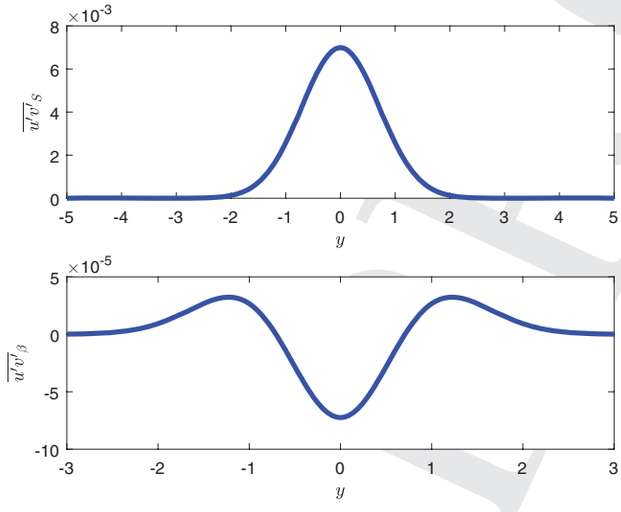

Figure 27.6 (a) The difference in momentum fluxes between a sheared and an unsheared wavepacket $\overline{u'v'}_S$ calculated over their life cycle when only the change in amplitude is taken into account. The wavenumber is $\sqrt{k^2 + l_0^2} = 1$, $h(y) = e^{-y^2/2}$, $|\theta_0| = 16°$, $|B| = 1$, $\delta U_y = 10^{-3}$ and $r = 0.1$. (b) The difference in momentum fluxes between a sheared and an unsheared wavepacket $\overline{u'v'}_\beta$ calculated over their life cycle when only the change in propagation is taken into account. $\beta = 0.1$ and the rest of the parameters are as in (a).

as a function of θ_t. A wavepacket starting in region II will propagate towards the north (see Fig. 27.4) but as shearing slows down the waves ($\eta_1 \sim -(\mathrm{d}A_M/\mathrm{d}l_t)$), the wavepacket will flux its momentum from southern latitudes compared to when it moved in the absence of the shear flow. This is shown in Fig. 27.5(b), illustrating the distribution of momentum flux of an unsheared and a sheared packet whose amplitudes are constant. Figure 27.6(b) plots this difference, $\overline{u'v'}_\beta$, and shows that the flux is downgradient in this case. The same happens for waves excited in region III, while the waves excited in regions I and IV produce up-gradient flux.

The net momentum fluxes produced by an ensemble of wavepackets will therefore depend on the spectral characteristics of the forcing that determine the regions I–IV in which the forcing has significant power. Bakas and Ioannou (2013b) showed that for the isotropic forcing (27.18),

$$\delta\langle u'v'\rangle = \\ = \frac{1}{2\pi}\int_{-\infty}^{\infty}\int_{-\infty}^{\infty}\overline{u'v'}_S \mathrm{d}\xi\mathrm{d}k + \frac{1}{2\pi}\int_{-\infty}^{\infty}\int_{-\infty}^{\infty}\overline{u'v'}_\beta \mathrm{d}\xi\mathrm{d}k \\ \simeq 0 - \frac{3\tilde{\varepsilon}\tilde{\beta}^2 r}{32\pi K_f^4}\frac{\mathrm{d}^3\delta U}{\mathrm{d}y^3}. \tag{27.30}$$

The first integral is zero, because the gain in momentum occurring for $|\theta_0| < \pi/6$ (waves excited in regions II and III) is fully compensated by the loss in momentum for $|\theta_0| > \pi/6$ (waves excited in regions I and IV), since for the isotropic forcing all possible wave orientations are equally excited. The net momentum fluxes are therefore produced by the $\overline{u'v'}_\beta$ term and are up-gradient, because the loss in momentum occurring for $|\theta_0| < \pi/6$, is over-compensated by the gain in momentum for $|\theta_0| > \pi/6$. The momentum fluxes are also proportional to the third derivative of δU, yielding a hyperdiffusive momentum flux divergence that tends to reinforce the mean flow and is therefore destabilizing. These destabilizing fluxes are proportional to $\tilde{\beta}^2$, and as a result the energy input rate required to form zonal jets increases as $1/\tilde{\beta}^2$ in this limit. It is worth noting that the first term integrates to zero only for the special case of the isotropic forcing, as even the slightest anisotropy yields a nonzero contribution from $\overline{u'v'}_S$. For example, consider the forcing covariance $\Xi(x_1, x_2, y_1, y_2) = \cos(k(x_1 - x_2))\, e^{-(y_1-y_2)^2/\delta^2}$ that mimics the forcing of the barotropic flow by the most unstable baroclinic wave, which has zero meridional wavenumber. In this case, the forcing that is centered at $l_0 = 0$ in wavenumber space injects significant power in a band of waves in regions II and III, and therefore $\overline{u'v'}_S$ yields up-gradient fluxes.

27.4.2 The Effects of the Change in the Mean Vorticity Gradient and the Finite Propagation Range

In order to take into account the effect of the change in the vorticity gradient, we retain higher-order terms with respect to $mL_f \ll 1$ in l_1 and η_1. In this case it can be shown that l_1 decreases with time at a rate proportional to $U_y(\xi) + U_{yyy}(\xi)$ (Bakas and Ioannou, 2013b). Since the local shear and the local change in the vorticity gradient have different signs, the wavepacket is "sheared less," and as a result we expect reduced momentum fluxes compared to the limit discussed in

Section 27.4.1. Indeed, for the isotropic forcing,

$$\delta \langle u'v' \rangle \simeq -\frac{3\tilde{\varepsilon}\tilde{\beta}^2 r}{32\pi K_{\rm f}^4}\left(\frac{{\rm d}^3\delta U}{{\rm d}y^3} - \frac{1}{4K_{\rm f}^2}\frac{{\rm d}^5\delta U}{{\rm d}y^5}\right). \tag{27.31}$$

That is, the change in the mean vorticity gradient has a stabilizing effect.

We finally relax the assumption that $\tilde{\beta} \ll 1$. In this case, l_1 and η_1 are affected by an integral shear and mean vorticity gradient over the region of propagation. For larger $\tilde{\beta}$, the wavepacket will encounter regions of both positive and negative shear, and as a result the momentum fluxes that are qualitatively proportional to the integral shear over the propagation region will be reduced. In the limit $\tilde{\beta} \gg 1$, the region of propagation is the whole sinusoidal flow with consecutive regions of positive and negative shear, and the integral shear along with the fluxes will asymptotically tend to zero. As a result, the energy input rate required for structural instability of zonal jets increases with $\tilde{\beta}$ in this limit.

27.5 EQUILIBRATION OF THE STRUCTURE-FORMING INSTABILITY AND SECONDARY INSTABILITIES AT FINITE AMPLITUDE

We now investigate the equilibration of the structure-forming instability by studying the S3T system of (27.9) and (27.12) discretized in a doubly periodic channel of size $2\pi \times 2\pi$. We approximate the monochromatic forcing (27.18) by considering the narrow-band forcing

$$\hat{\Xi}(k,l) = \frac{K_{\rm f}}{\Delta K_{\rm f}}\begin{cases} 1 & \text{for } |\sqrt{k^2+l^2} - K_{\rm f}| \le \Delta K_{\rm f}, \\ 0 & \text{for } |\sqrt{k^2+l^2} - K_{\rm f}| > \Delta K_{\rm f}, \end{cases} \tag{27.32}$$

where k, l assume integer values, which injects energy at rate ε in a narrow ring in wavenumber space with radius $K_{\rm f}$ and width $\Delta K_{\rm f}$. We consider the set of parameter values $\beta = 10$, $r = 0.01$, $\nu = 1.19 \times 10^{-6}$, $K_{\rm f} = 10$ and $\Delta K_{\rm f} = 1$, for which $\tilde{\beta} = 100$. The integration is therefore in the parameter region of Fig. 27.1 in which the nonzonal structures are more unstable than the zonal jets. The growth rates of the coherent structures for integer values of the wavenumbers n and m are calculated from the discrete version of (27.15) obtained by substituting the integrals with sums over integer values of the wavenumbers (Bakas and Ioannou, 2013a).

We investigate the equilibration of the instability by studying the evolution of the S3T system as we increase the energy input rate $\tilde{\varepsilon}$. Consider first the supercritical energy input rate $\tilde{\varepsilon} = 4\tilde{\varepsilon}_{\rm c}$. For these parameters only nonzonal modes are unstable, with the perturbation with $(n,m) = (1,5)$ growing the most. At $t = 0$, we introduce a small random perturbation, whose stream function is shown in Fig. 27.7(a). After a few e-folding times, a harmonic structure of the form $Z = \cos(x)\cos(5y)$ dominates the large-scale flow. The energy of this large-scale structure, shown in Fig. 27.7(b), increases rapidly and eventually saturates. At this point the large-scale flow gets attracted to a traveling wave finite-amplitude equilibrium structure – see Fig. 27.7(c) – close in form to the harmonic $Z = \cos(x)\cos(5y)$ that propagates westward. This is

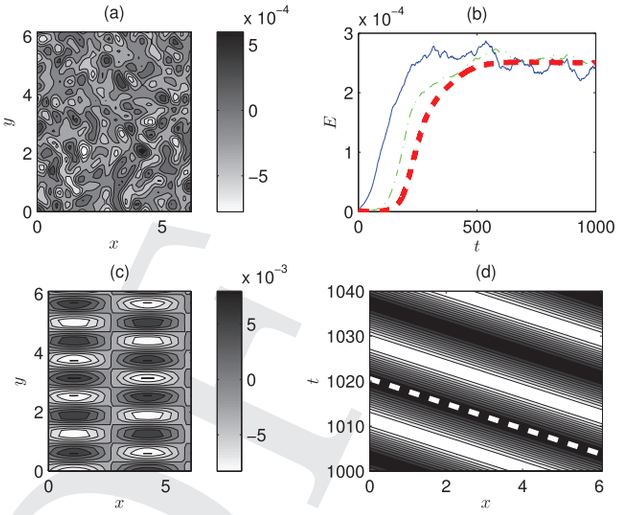

Figure 27.7 Equilibration of the S3T instabilities. (a) Stream function of the initial perturbation. (b) Energy evolution of the initial perturbation shown in panel (a) as obtained from the integration of the S3T equations (27.9) and (27.12) (dashed line) and from the integration of the ensemble quasi-linear (EQL) system (27.4)–(27.3) with $N_{\rm ens} = 10$ (solid line) and $N_{\rm ens} = 100$ (dash-dotted line) ensemble members that is discussed in Section 27.6. (c) Snapshot of the stream function $\Psi_{\rm eq}$ of the traveling wave structure and (d) Hovmöller diagram of $\Psi_{\rm eq}(x, y = \pi/4, t)$ for the finite equilibrated traveling wave. The thick dashed line shows the phase speed obtained from the stability equation, (27.15). The energy input rate is $\tilde{\varepsilon} = 4\tilde{\varepsilon}_{\rm c}$ and $\tilde{\beta} = 100$. Adapted from Bakas and Ioannou (2013c). © Cambridge University Press. Reprinted with permission.

illustrated in the Hovmöller diagram of $\psi(x, y = \pi/4, t)$ shown in 27.7(d). The sloping dashed line in the diagram corresponds to the phase speed of the traveling wave, which is found to be approximately the phase speed of the unstable $(n,m) = (1,5)$ eigenmode.

Consider now the energy input rate $\tilde{\varepsilon} = 10\tilde{\varepsilon}_{\rm c}$. While the maximum growth rate still occurs for the $(|n|,|m|) = (1,5)$ nonzonal structure, zonal jet perturbations are unstable as well ($\tilde{\varepsilon}_{\rm cz} = 5.2\varepsilon_{\rm c}$). If the S3T dynamics are restricted to account only for the interaction between zonal flows and turbulence by employing a zonal mean rather than an ensemble mean, an infinitesimal jet perturbation will grow and equilibrate at finite amplitude. To illustrate this we integrate the S3T dynamical system (27.20)–(27.21) restricted to zonal flow coherent structures. The energy of the small zonal jet perturbation $\delta Z = 0.1\cos(4y)$ is shown in Fig. 27.8 to grow and saturate at a constant value, and the stream function of the equilibrated jet is shown in the left inset of Fig. 27.8. However, in the context of the generalized S3T analysis that takes into account the dynamics of the interaction between coherent nonzonal structures and jets, we find that these S3T jet equilibria are saddles: stable to zonal jet perturbations but unstable to nonzonal perturbations. To show this, we consider the evolution of the same jet perturbation $\delta Z = 0.1\cos(4y)$ under the generalized S3T dynamics (27.9) and (27.12), and find that the flow follows the zonally restricted S3T dynamics and equilibrates to the same finite-amplitude zonal jet (Fig. 27.8). At this point we insert a small

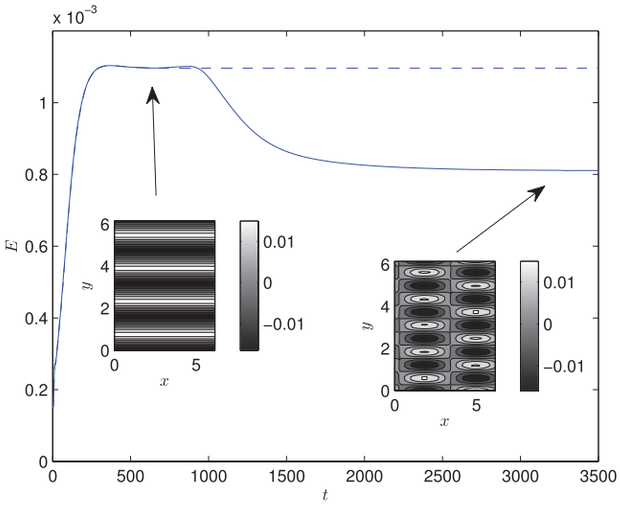

Figure 27.8 Energy evolution of an initial jet perturbation $\delta Z = 0.1\cos(4y)$ for the zonally restricted S3T dynamics (27.20)–(27.21) (dashed line) and the generalized S3T dynamics (27.9) and (27.12) (thin line). The insets show a snapshot of the mean flow stream function at $t = 700$ (left) and the stream function of the equilibrated structure at $t = 3500$ (right) under the generalized S3T dynamics. The parameters are $\tilde{\varepsilon} = 10\tilde{\varepsilon}_c$ and $\tilde{\beta} = 100$.

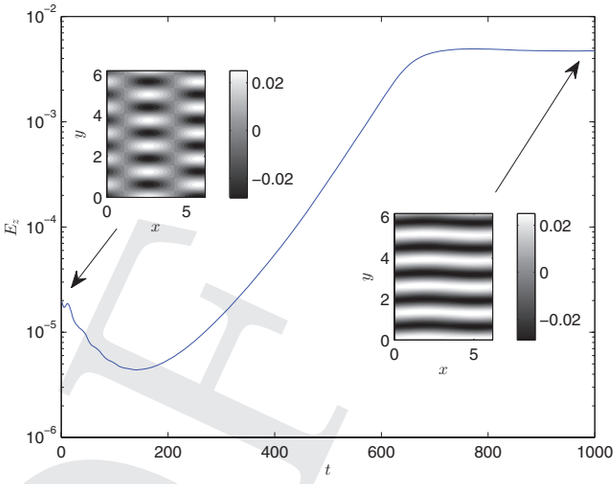

Figure 27.9 Zonal energy evolution of a random zonal perturbation imposed on the nonzonal traveling wave equilibrium shown in the left inset. The stream function of the equilibrated structure is shown in the right inset. The energy input rate is $\tilde{\varepsilon} = 30\tilde{\varepsilon}_c$ and $\tilde{\beta} = 100$.

random perturbation to the equilibrated flow. Soon after, nonzonal undulations grow and the flow transitions to the stable $Z = \cos(x)\cos(5y)$ traveling wave state that is also shown in Fig. 27.8. As a result, the finite equilibrium zonal jet structure is S3T unstable to coherent nonzonal perturbations and is not expected to appear in nonlinear simulations despite the fact that the zero flow equilibrium is unstable to zonal jet perturbations. A thorough investigation of this S3T instability of zonal jet equilibria at finite amplitude can be found in Constantinou et al. (2016). It was found that the large-scale waves with $n \neq 0$ exist as damped external Rossby wave modes of the linear dynamics operator $A^e(U^e)$ around the zonal jet equilibrium with velocity U^e. These external modes have a structure so as to extract energy from the mean jet, but the energy extraction is not sufficient to overcome dissipation and these modes are stable in the absence of turbulence. The S3T instability occurs in this case as there is a slight change in the wave structure mediated by the Reynolds stress feedback, through which the waves are able to tap more energy from the mean jet and become S3T unstable. This mechanism is distinct from the eddy–mean flow dynamics of the jet-forming instability discussed in the previous section. In the latter case, the infinitesimal jet interacts with the turbulent eddies and is able to extract energy from the turbulence through the Reynolds stress feedback. In this case, the turbulent eddies merely mediate the change in the nonzonal wave structure and the wave is able to extract more energy from the mean flow and not from the turbulence.

Finally, consider the case $\tilde{\varepsilon} = 30\tilde{\varepsilon}_c$. At this energy input rate, the finite-amplitude nonzonal traveling wave equilibria become S3T unstable. To show this, we consider the nonzonal traveling wave equilibrium obtained by the evolution of the small nonzonal perturbation $\delta Z = 0.01\cos(x)\cos(5y)$ to the homogeneous state that is shown in the left inset of Fig. 27.9 and impose a small random zonal perturbation. The evolution of the zonal energy $E_z = (1/2)\overline{U}^2$, where the overbar denotes a zonal average, is shown in Fig. 27.9. After an initial transition period, the zonal perturbations grow exponentially and the flow transitions to the jet equilibrium state shown in the right inset of Fig. 27.9. Note, however, that the jet equilibrium structure is not zonally symmetric. This is a new type of S3T equilibrium: it is a mix between a zonal jet and a nonzonal traveling wave with the same meridional scale. These mixed equilibria appear to be the attractors for larger energy input rates as well. This is illustrated in Fig. 27.10, showing the structure of the mixed equilibrium at $\varepsilon = 50\varepsilon_c$. The equilibrium structure consists of a large-amplitude zonally symmetric jet with larger scale compared to the mixed state in Fig. 27.9. Embedded in it are nonzonal vortices with the same meridional scale and with about 14% the energy of the zonal jet. These vortices, shown in Fig. 27.10(b), have approximately the compact support structure $\Psi = \cos(x)\cos(4y)$ and propagate westward, as shown in the Hovmöller diagram in Fig. 27.10(c). This instability of the finite-amplitude traveling wave states was numerically found to occur for $\tilde{\varepsilon} > \tilde{\varepsilon}_{NL} = 15\tilde{\varepsilon}_c$. To summarize, for slightly supercritical energy input rates, the S3T system is attracted to finite-amplitude propagating wave states that have the characteristics of the nonzonal unstable modes of the homogeneous equilibrium. For energy input rates $\tilde{\varepsilon}_{NL} > \tilde{\varepsilon} > \tilde{\varepsilon}_{cz}$, for which the homogeneous equilibrium is unstable to both zonal and nonzonal structures, the S3T dynamics are still attracted to the traveling wave states, as the finite-amplitude zonal jet equilibria are unstable to non-zonal mean flow perturbations. For $\tilde{\varepsilon} > \tilde{\varepsilon}_{NL}$ the traveling wave state equilibria are unstable to zonal flow perturbations and the S3T system is attracted to mixed states with small-amplitude traveling waves embedded within large-amplitude zonal jets.

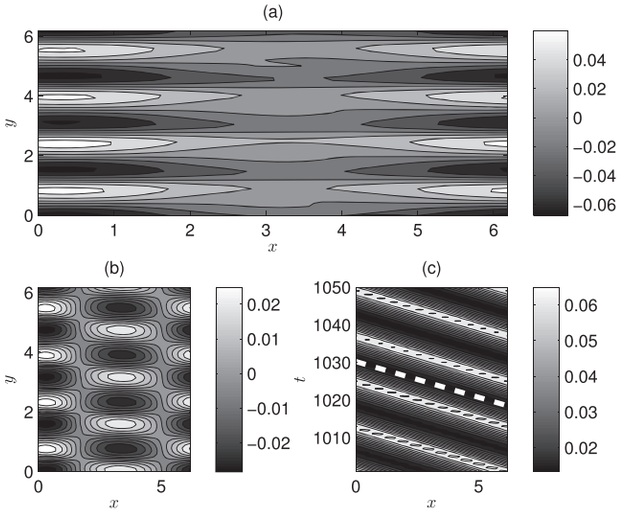

Figure 27.10 Mixed zonal jet–traveling wave S3T equilibrium for $\tilde{\varepsilon} = 50\tilde{\varepsilon}_c$ and $\tilde{\beta} = 100$. (a) Snapshot of the stream function Ψ_{eq} of the equilibrium state. (b) Contour plot of the nonzonal component $\Psi_{eq} - \overline{\Psi_{eq}}$ of the equilibrium structure, where the overline denotes a zonal average. (c) Hovmöller diagram of $\Psi_{eq}(x, y = \pi/4, t)$ for the equilibrated structure.

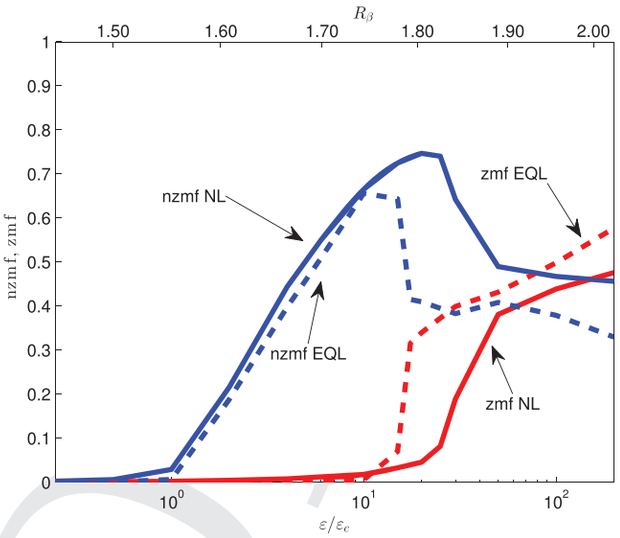

Figure 27.11 The zmf and nzmf indices defined in (27.33) and (27.35), respectively, as functions of energy input rate $\varepsilon/\varepsilon_c$ and the zonostrophy parameter R_β for the nonlinear (NL) integrations and an ensemble of quasi-linear (EQL) integrations (dashed line) with $N_{ens} = 10$ ensemble members as described in the text. The critical value $\varepsilon_c = 8.4 \times 10^{-6}$ is the energy input rate at which the S3T predicts structural instability of the homogeneous turbulent state. Zonal jets emerge for $\varepsilon > \varepsilon_{nl}$, with $\varepsilon_{nl} = 15\varepsilon_c$. The parameters are $\beta = 10$, $r = 0.01$ and $\nu = 1.19 \times 10^{-6}$, and the forcing is an isotropic ring in wavenumber space with radius $K_f = 10$ and width $\Delta K_f = 1$.

27.6 COMPARISON WITH ENSEMBLE MEAN QUASI-LINEAR AND NONLINEAR SIMULATIONS

27.6.1 Comparison with an Ensemble of Quasi-Linear Simulations

Within the context of the second-order cumulant closure, the S3T formulation allows the identification of statistical turbulent equilibria in the infinite ensemble limit, in which the fluctuations induced by the stochastic forcing are averaged to zero. However, these S3T equilibria and their stability properties ~~are~~ manifest even in single realizations of the turbulent system. For example, previous studies using S3T obtained zonal jet equilibria in barotropic, shallow-water and baroclinic flows in close correspondence with observed jets in planetary flows (Farrell and Ioannou, 2007, 2008, 2009a,c). In addition, previous studies of S3T dynamics restricted to the interaction between zonal flows and turbulence in a β-plane channel showed that when the energy input rate is such that the zero mean flow equilibrium is unstable, zonal jets also appear in the nonlinear simulations with the structure (scale and amplitude) predicted by S3T (Srinivasan and Young, 2012; Constantinou et al., 2014a).

A very useful intermediate model that retains the wave–mean flow dynamics of the S3T system while relaxing the infinite ensemble approximation is the quasi-linear system (27.5)–(27.6). Under the ergodic assumption, this can be interpreted as an ensemble of quasi-linear equations (EQL) in which the ensemble mean can be calculated from a finite number of ensemble members. Its integration is done as follows. A pseudo-spectral code with 128×128 resolution and a fourth-order Runge–Kutta scheme for time-stepping is used to integrate (27.5)–(27.6) forward. At each time step, N_{ens} separate integrations of (27.6) are performed with the eddies evolving according to the instantaneous flow. Then, the ensemble average vorticity flux divergence is calculated as the average over the N_{ens} simulations and (27.5) is stepped forward in time according to those fluxes. The EQL system reaches a statistical equilibrium at timescales of the order of $t_{eq} \sim O(1/r)$, and the integration was carried on until $t = 100 t_{eq}$ in order to collect accurate statistics.

We choose the same parameter values as in the S3T integrations in Section 27.5 ($\beta = 10$, $r = 0.01$, $\nu = 1.19 \times 10^{-6}$, $K_f = 10$ and $\Delta K_f = 1$). For these parameters (and $\tilde{\beta} = 100$), S3T predicts the emergence of propagating nonzonal structures when the energy input rate exceeds the critical threshold $\tilde{\varepsilon}_c$, and the emergence of mixed zonal jet–traveling wave states when the finite-amplitude traveling wave states become structurally unstable to zonal jet perturbations. In order to examine whether the same bifurcations occur in the EQL system, we consider two indices that measure the power concentrated at scales larger than the scales forced. The first is the zonal mean flow index defined, as in Srinivasan and Young (2012), as the ratio of the energy of zonal jets with scales larger than the scale of the forcing over the total energy,

$$\text{zmf} = \frac{\sum_{l:l<K_f-\Delta K_f} \hat{E}(k=0,l)}{\sum_{kl} \hat{E}(k,l)}, \tag{27.33}$$

where

$$\hat{E}(k,l) = \frac{1}{2T} \int_0^T \left(\left\langle \frac{|\hat{\zeta}'|^2}{k^2+l^2} \right\rangle + \frac{|\hat{Z}|^2}{k^2+l^2} \right) \mathrm{d}t \tag{27.34}$$

is the time-averaged total energy power spectrum of the flow at wavenumbers (k, l). The second is the nonzonal mean flow

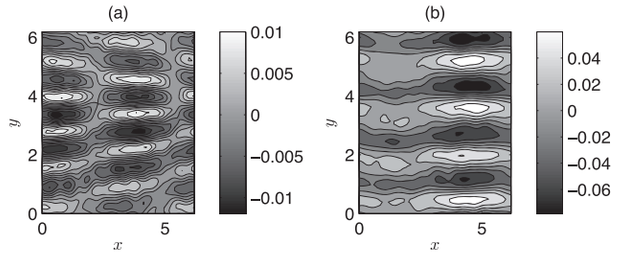

Figure 27.12 Snapshot of the mean stream function Ψ at statistical equilibrium obtained from the ensemble mean quasi-linear simulations with $N_{\rm ens} = 10$ members for $\varepsilon = 4\varepsilon_{\rm c}$ (a) and $\varepsilon = 50\varepsilon_{\rm c}$ (b). The parameters are as in Fig. 27.11.

index defined as the ratio of the energy of the nonzonal modes with scales larger than the scale of the forcing over the total energy:

$$\text{nzmf} = \frac{\sum_{kl:K<K_{\rm f}-\Delta K_{\rm f}} \hat{E}(k,l)}{\sum_{kl} \hat{E}(k,l)} - \text{zmf}. \tag{27.35}$$

If the structures that emerge are coherent, then the nzmf and the zmf indices quantify the amplitude of the nonzonal and the zonal coherent structures, respectively. Figure 27.11 shows both indices as a function of the energy input rate ε and as a function of the corresponding values of the zonostrophy index R_β for EQL simulations with $N_{\rm ens} = 10$ members. The rapid increase of the nzmf index for $\varepsilon > \varepsilon_{\rm c}$ (corresponding to $R_\beta > 1.55$) illustrates that this regime transition in the flow predicted by S3T with the emergence of nonzonal structures manifests in the quasi-linear dynamics as well. We now consider the case $\varepsilon = 4\varepsilon_{\rm c}$ in detail, with the traveling wave structure $Z = \cos(x)\cos(5y)$ maintained in the S3T integrations. We observe that the S3T equilibria manifest in the EQL simulations with the addition of some "thermal noise" due to the stochasticity of the forcing that is retained in this system. This is illustrated in Fig. 27.7(b), showing the energy growth of the coherent structure for $N_{\rm ens} = 10$ and $N_{\rm ens} = 100$. The energy of the coherent structure in the EQL integrations fluctuates around the values predicted by the S3T system, with the fluctuations decreasing as $1/\sqrt{N_{\rm ens}}$. However, even with only 10 ensemble members we get an estimate that is very close to the theoretical estimate of the infinite ensemble members obtained from the S3T integration. The structure of the traveling wave equilibrium in the quasi-linear simulations shown in Fig. 27.12(a) and its phase speed (not shown) are also in very good agreement with the corresponding structure and phase speed obtained from the S3T integration.

As discussed in the previous section, the flow stays on the attractor of the nonzonal traveling wave states for $\varepsilon \le \varepsilon_{\rm nl}$. When $\varepsilon > \varepsilon_{\rm nl}$ the nonzonal traveling wave equilibria become S3T unstable, while at these parameter values the S3T system has mixed zonal jet–traveling wave equilibria that are stable (cf. Fig. 27.10). The rapid increase in the zmf index with the concomitant rapid decrease in the nzmf index shown in Fig. 27.11 illustrates that this regime transition manifests in the EQL system as well with similar mixed zonal–traveling wave states appearing. The structure of the mixed zonal jet–traveling wave equilibrium for $\varepsilon = 50\varepsilon_{\rm c}$ is shown in Fig. 27.12(b) and, similar to the S3T equilibrium in Fig. 27.10, it consists mainly of four zonal jets and the compact support vortices $Z \sim \cos(x)\cos(4y)$ embedded in the jets. We therefore conclude that the EQL system accurately captures the characteristics of the emerging structures and presents a useful model, not only because it includes the thermal effect of the finite number of ensemble members but also because it provides a computationally efficient model of the S3T dynamics in comparison with the S3T dynamical system, which for an $M \times M$ resolution requires the algebraic manipulation of the M^4 covariance matrix C.

27.6.2 Comparison with Nonlinear Simulations

In order to compare the predictions of S3T with nonlinear simulations, we solve (27.1) with the narrow-band forcing (27.32) on a doubly periodic channel of size $2\pi \times 2\pi$ using the same pseudo-spectral code as in the EQL simulations and the same parameter values. Figure 27.11 shows the nzmf and zmf indices as a function of the energy input rate ε for the NL simulations. The rapid increase in the nzmf index for $\varepsilon > \varepsilon_{\rm c}$ shows that the nonlinear dynamics share the same bifurcation structure as the S3T statistical dynamics. In addition, the stable S3T equilibria are, in principle, viable repositories of energy in the turbulent flow, and the nonlinear system is expected to visit their attractors for finite time intervals. Indeed, for $\varepsilon = 4\varepsilon_{\rm c}$ the pronounced peak at $(|k|,|l|) = (1,5)$ of the time-averaged power spectrum shown in Fig. 27.13(a) illustrates that the traveling wave equilibrium with $(|k|,|l|) = (1,5)$ that emerges in the S3T integrations is the dominant structure in the NL simulations. Comparison of the energy spectra obtained from the EQL and the NL simulations (not shown) reveals that the amplitude of this structure in the quasi-linear and in the nonlinear dynamics almost matches. Remarkably, the phase speed of the S3T traveling wave matches the corresponding phase speed of the $(|k|,|l|) = (1,5)$ structure observed in the NL simulations, as can be seen in the Hovmöller diagram in Fig. 27.13(b). Such an agreement in the characteristics of the emerging structures between the EQL and NL simulations occurs for a wide range of energy input rates, as can be seen by comparing the nzmf indices in Fig. 27.11. As a result, S3T predicts the dominant nonzonal propagating structures in the nonlinear simulations, as well as their amplitude and phase speed.

We now focus on the second regime transition with the emergence of zonal jets. The increase in the zmf index in the NL simulations for $\varepsilon > \varepsilon_{\rm nl}$ that is shown in Fig. 27.11 indicates the emergence of jets roughly at the bifurcation point of the S3T and EQL simulations. However, the energy input rate threshold for the emergence of jets is larger in the NL simulations compared to the corresponding EQL threshold. This discrepancy possibly occurs due to the fact that the exchange of instabilities between the mixed jet–traveling wave equilibria and the pure traveling wave equilibria depends on the equilibrium structure $[Z^{\rm E}, C^{\rm E}]$. Small changes, for example, in $C^{\rm E}$ that might be caused by the eddy–eddy terms neglected in S3T can cause the exchange of instabilities to occur at slightly different energy input rates. It was shown in a recent study that when the effect of the eddy–eddy terms is taken into account by obtaining $C^{\rm E}$ directly from the nonlinear simulations, the S3T stability analysis performed on the corrected equilibrium states accurately predicts the energy input rate for the emergence of jets in the

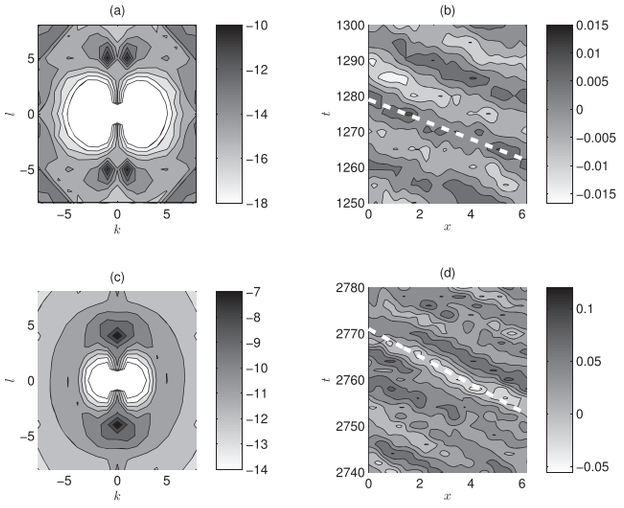

Figure 27.13 Time-averaged energy power spectra, $\log(\hat{E}(k,l))$, obtained from the nonlinear simulation of (27.1) at $\varepsilon/\varepsilon_c = 4$ (a) and $\varepsilon/\varepsilon_c = 50$ (c). Also shown are Hovmöller diagrams of $\psi(x, y = \pi/4, t)$ at $\varepsilon/\varepsilon_c = 4$ (b) and $\varepsilon/\varepsilon_c = 50$ (d). The thick dashed lines correspond to the phase speed obtained from the eigenvalue relation (27.15). Adapted from Bakas and Ioannou (2013c). © Cambridge University Press. Reprinted with permission.

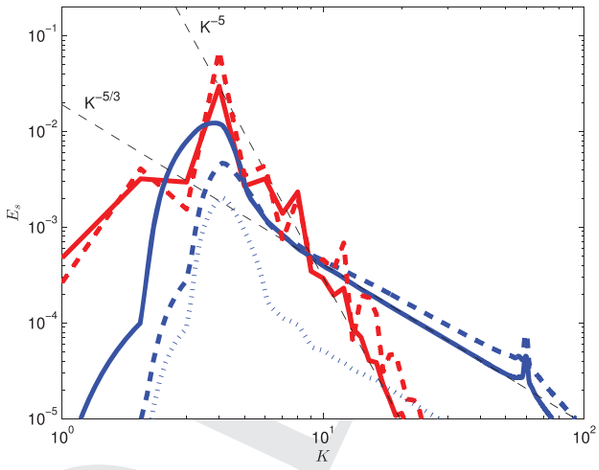

Figure 27.14 Residual (blue) and zonal (red) energy spectra for the NL (solid) and EQL (dashed) simulations in the zonostrophic regime. Also shown are the residual spectra from the EQL simulations when only the coherent motions are taken into account (blue dotted line). The parameters are $K_f = 60$, $\Delta K = 1$, $\beta = 42$, $r = 0.01$ and $\varepsilon = 0.0065$, for which $\tilde{\beta} = 70$, $\tilde{\varepsilon} = 7308\tilde{\varepsilon}_c$, $k_\beta = 12.9$ and $R_\beta = 2.5$. Lines (thin dashed) of slope $K^{-5/3}$ and K^{-5} are also plotted for reference. The pseudo-spectral code was run with a 512×512 resolution and the exponential filter of Smith et al. (2002) instead of hyperdiffusion.

nonlinear simulations (Constantinou et al., 2014a). The power spectrum obtained from the NL simulations for $\varepsilon = 50\varepsilon_c$ shows an energy peak at $(k, |l|) = (0, 4)$, with secondary power peaks at $(|k|, |l|) = (1, 4)$ and $(|k|, |l|) = (1, 5)$ of approximately 12% of the energy in the zonal jet each. The Hovmöller diagram of the stream function shown in Fig. 27.13(d) reveals that the dominant nonzonal structures in the NL simulations propagate in the retrograde direction. As a result, the mixed S3T equilibrium of Fig. 27.10 manifests in the NL simulations. Note, however, that the phase speed calculated from the diagram is different from the phase speed of the $(|k|, |l|) = (1, 4)$ structure in Fig. 27.10. At larger energy input rates the zonal jets have typically larger scales due to jet merging, and coexist with energetically significant westward-propagating nonzonal structures having an energy of 10%–50% of the jet energy and scales $(|k|, |l|) = (1, m)$, where m is the number of jets in the channel. Such an agreement again holds for a wide range of energy input rates, as the zmf indices obtained from the EQL and the NL simulations indicate. In summary, S3T predicts the characteristics of both nonzonal propagating structures and of zonal jets in the nonlinear simulations.

27.6.3 Zonostrophic Regime

S3T and the corresponding ensemble quasi-linear system were obtained by ignoring the eddy–eddy nonlinear interactions. Therefore, the question arises as to whether the predictions of S3T are useful in the zonostrophic regime. In this regime, which is highly supercritical with respect to S3T instability of the homogeneous equilibrium (sees Fig. 27.1), maintenance of zonal jets and zonons were interpreted by previous studies to arise from an inverse energy cascade (Galperin et al., 2010), a highly nonlinear process, which is absent in S3T. According to this interpretation, the turbulent energy cascades isotropically toward large scales until it reaches k_β. At this scale the cascade becomes anisotropic and most of the energy is channelled into the zonal flows. To illustrate this, the time-averaged energy power spectra $\hat{E}(k, l)$ are typically split between the zonal spectra $\hat{E}_z(l) = \hat{E}(k = 0, l)$ and the residual $\hat{E}_R(k, l) = \hat{E} - \hat{E}_z$. The zonal and residual spectra calculated from NL integrations in the zonostrophic regime ($K_f = 60$, $\Delta K = 1$, $\beta = 42$, $r = 0.01$, $\varepsilon = 0.0065$) are shown in Fig. 27.14. Up to the scale k_β, the residual spectra follow the Kolmogorov $K^{-5/3}$ law in accordance with an isotropic cascade assumption. At this scale, the cascade is anisotropized and the residual spectra steepen. However, most of the energy is in zonal scales, with the zonal spectra following a much steeper K^{-5} law.

The residual and the zonal spectra obtained from an EQL simulation with $N_{ens} = 10$ for the same parameters are also shown in Fig. 27.14. The residual spectra follow a slope shallower than $K^{-5/3}$ for $K > k_\beta$, while they steepen after k_β and reach a lower peak with respect to the corresponding spectra from the NL simulations. In addition, the residual part of the spectrum corresponds mainly to incoherent motions for scales with $K > k_\beta$. This is revealed by taking into account only the spectra of the coherent part of the flow and calculating the residual spectrum, which is also shown in Fig. 27.14. For most of the scales, it is at least one to two orders of magnitude lower than the corresponding residual spectrum when both coherent and incoherent motions are taken into account, and only the nonzonal structures with large scales (close to the energy peak) appear to be coherent. The failure of the EQL simulations to exactly reproduce the $K^{-5/3}$ slope of the incoherent turbulent motions is not surprising, since the inverse energy cascade that is absent in the EQL simulations is essential for this part of

the spectrum. The energetically important part, however, which contains the large-scale energetic waves, is captured by the EQL simulations. The zonal spectra obtained from the EQL simulations follow the same K^{-5} law and peak at the same scale compared to the NL simulations, but the peak has a larger amplitude.

So, to summarize, the scale and the shape of the dominant jet structure, as well as the scale of the most energetic coherent nonzonal structures, are accurately captured by the EQL simulations. The eddy–eddy interactions neglected in the EQL simulations appear to only set the proper scaling for the tail of the spectrum that consists of incoherent turbulent motions and change the partition between the energy of the jet (which is overestimated in the EQL simulations) and that of the nonzonal large-scale structures (which is underestimated in the EQL simulations).

27.7 SUMMARY AND DISCUSSION

This chapter has addressed the emergence of coherent structures in barotropic β-plane turbulence using the tools of Stochastic Structural Stability Theory (S3T), a theory that expresses the statistics of the turbulent flow dynamics as a systematic cumulant expansion truncated at second order. With the interpretation of the ensemble average as a Reynolds average over the fast turbulent eddies adopted in this contribution, the second-order cumulant expansion results in a closed, nonlinear dynamical system that governs the joint evolution of slowly varying, spatially localized coherent structures with the second-order statistics of the rapidly evolving turbulent eddies. The fixed points of this autonomous, deterministic nonlinear system define statistical equilibria, the stability of which are amenable to the usual treatment of linear and nonlinear stability analysis.

The linear stability of the homogeneous S3T equilibrium with no mean velocity was examined analytically for the case of an isotropic random stirring at scale L_f that sustains the turbulence in the barotropic flow, which reaches a steady state in the presence of linear dissipation at a rate r. Structural instability was found to occur for perturbations with smaller scale than the forcing, when the energy input rate $\tilde{\varepsilon} = \varepsilon/(r^3 L_\mathrm{f}^2)$ is larger than a certain threshold $\tilde{\varepsilon}_\mathrm{c}$ that depends on $\tilde{\beta} = \beta L_\mathrm{f}/r$. It was found that when $\tilde{\beta}$ is small or of order one, the maximum growth rate occurs for stationary zonal structures, while for large $\tilde{\beta}$, westward-propagating nonzonal structures grow the most.

The eddy–mean flow dynamics underlying the S3T instability of zonal jets was then studied in detail. It was shown that, close to the structural stability boundary, the dynamics can be split into two competing processes. The first, which is shearing of the eddies by the local shear described by Orr dynamics in the β plane, was shown to lead to jet-forming up-gradient momentum fluxes acting exactly as negative viscosity for an anisotropic forcing and as negative hyperviscosity for isotropic forcing. The second, which is momentum flux divergence resulting from lateral wave propagation on the nonuniform local mean vorticity gradient, was shown to lead to jet-opposing down-gradient fluxes acting as hyperdiffusion.

The equilibration of the unstable, exponentially growing coherent structures for large $\tilde{\beta}$ was then studied through numerical integrations of the S3T dynamical system. When the forcing amplitude is slightly supercritical, the finite-amplitude traveling wave equilibrium has a structure close to the corresponding unstable nonzonal perturbation with the same scale. When the forcing amplitude is highly supercritical, the instabilities equilibrate to mixed states consisting of strong zonal jets with smaller-amplitude traveling waves embedded in them.

The predictions of S3T were then compared with the results obtained from direct numerical simulations of the turbulent dynamics. The critical threshold above which coherent nonzonal structures are unstable according to the stability analysis of the S3T system was found to be in excellent agreement with the critical value above which nonzonal structures acquire significant power in the nonlinear simulations. The scale, phase speed and amplitude of the dominant structures in the nonlinear simulations were also found to correspond to the structures predicted by S3T. In addition, the threshold for the emergence of jets, which is identified in S3T as the energy input rate at which an S3T stable, finite-amplitude zonal jet equilibrium exists, was found to roughly match the corresponding threshold for jet formation in the nonlinear simulations, with the emerging jet scale and amplitude being accurately obtained using S3T. Such good agreement between the predictions of S3T and direct numerical simulations holds not only close to the bifurcation point for the emergence of coherent structures but also in the regime of zonostrophic turbulence. Consequently, these results provide a concrete example that large-scale structure in barotropic turbulence, whether it is zonal jets or nonzonal coherent structures, emerges and is sustained from systematic self-organization of the turbulent Reynolds stresses by spectrally nonlocal interactions and in the absence of a turbulent cascade.

APPENDICES

27.A BOUNDEDNESS OF THE SOLUTIONS AND INVARIANTS OF THE S3T EQUATIONS

The S3T system in the absence of forcing and dissipation has similar quadratic invariants to the nonlinear system. Further, the solutions of the S3T equations remain bounded for all times. That is, the sum of the enstrophy of the ensemble mean over the domain, $H_\mathrm{m} = 1/2 \int Z^2 \mathrm{d}x\mathrm{d}y$, and the eddy enstrophy over the domain, $H_\mathrm{p} = 1/2 \int C_{\mathbf{x}_1=\mathbf{x}_2} \mathrm{d}x\mathrm{d}y$, is conserved. Similarly, the sum of the energy of the ensemble mean, $E_\mathrm{m} = 1/2 \int (U^2 + V^2) \mathrm{d}x\mathrm{d}y$, and the eddy energy, $E_\mathrm{p} = 1/2 \int (\Delta_1^{-1} C)_{\mathbf{x}_1=\mathbf{x}_2} \mathrm{d}x\mathrm{d}y$, is also conserved. We show this by first multiplying (27.9) (in the absence of hyperdiffusion) by Z to obtain

$$\partial_t \eta_\mathrm{m} + U\partial_x \eta_\mathrm{m} + V\partial_y \eta_\mathrm{m} + \beta V Z = -Z\nabla\cdot\langle \mathbf{u}'\zeta'\rangle - 2r\eta_\mathrm{m}, \quad (27.\mathrm{A}.1)$$

where $\eta_\mathrm{m} = Z^2/2$ is the enstrophy density of the ensemble mean. Integrating by parts and using the continuity equation, we rewrite the advection terms as

$$U\partial_x \eta_\mathrm{m} + V\partial_y \eta_\mathrm{m} = \partial_x(U\eta_\mathrm{m}) + \partial_y(V\eta_\mathrm{m}). \quad (27.\mathrm{A}.2)$$

Writing $Z = \partial_x V - \partial_y U$ and again using the continuity equation, we have

$$ZV = \partial_x \frac{U^2 + V^2}{2} - \partial_y(UV), \quad (27.\mathrm{A}.3)$$

and (27.A.1) becomes

$$\partial_t \eta_\mathrm{m} + \nabla\cdot(\mathbf{U}\eta_\mathrm{m}) + \beta\partial_x e_\mathrm{m} - \beta\partial_y(UV) = -Z\nabla\cdot\langle\mathbf{u}'\zeta'\rangle - 2r\eta_\mathrm{m}, \tag{27.A.4}$$

where $e_\mathrm{m} = (1/2)(U^2+V^2)$ is the energy density of the ensemble mean. Similarly, it can be shown from (27.12) that the ensemble mean of the eddy enstrophy density $\eta_\mathrm{p} = (1/2)C_{\mathbf{x}_1=\mathbf{x}_2}$ evolves (in the absence of hyperdiffusion) according to

$$\partial_t \eta_\mathrm{p} + \nabla\cdot(\mathbf{U}\eta_\mathrm{p}) + \beta\left[\partial_x(e_\mathrm{p}) - \partial_y\langle u'v'\rangle\right] + \\ + \langle u'\zeta'\rangle\partial_x Z + \langle v'\zeta'\rangle\partial_y Z = \eta_\mathrm{f} - 2r\eta_\mathrm{p}, \tag{27.A.5}$$

where $e_\mathrm{p} = (1/2)(\Delta_1^{-1}C)_{\mathbf{x}_1=\mathbf{x}_2}$ is the ensemble mean of the eddy energy density and $\eta_\mathrm{f} = (1/2)\Xi_{\mathbf{x}_1=\mathbf{x}_2}$ is the enstrophy density of the forcing. Adding (27.A.4) and (27.A.5), we obtain the equation for the evolution of the total enstrophy density $\eta = \eta_\mathrm{p}+\eta_\mathrm{m}$:

$$(\partial_t + 2r)\eta - \eta_\mathrm{f} = -\nabla\cdot(\mathbf{U}\eta) - \beta\partial_x(e_\mathrm{p}+e_\mathrm{m}) + \beta\partial_y(UV + \langle u'v'\rangle). \tag{27.A.6}$$

Integrating (27.A.6) over the horizontal domain, the terms on the right-hand side of (27.A.6) integrate to zero and the total enstrophy $H = H_\mathrm{m}+H_\mathrm{p} = \int(\eta_\mathrm{m}+\eta_\mathrm{p})\mathrm{d}x\mathrm{d}y$ evolves according to

$$\partial_t H = H_\mathrm{f} - 2rH, \tag{27.A.7}$$

where H_f is the total enstrophy imparted by the forcing. As a result, the enstrophy is bounded and has the value $H^\mathrm{eq} = H_\mathrm{f}/(2r)$ at steady state. Similarly, it can be shown that the total energy $E = E_\mathrm{m} + E_\mathrm{p}$ is bounded.

27.B CALCULATION OF THE DISPERSION RELATION AND ITS PROPERTIES

In this appendix we derive the dispersion relation (27.15), which determines the stability of zonal as well as nonzonal perturbations in homogeneous turbulence. We follow closely the treatment of Srinivasan and Young (2012). We first rewrite (27.9) and (27.12) in terms of the variables $\tilde{x} = x_1 - x_2$, $\overline{x} = (1/2)(x_1+x_2)$, $\tilde{y} = y_1 - y_2$ and $\overline{y} = (1/2)(y_1+y_2)$. The derivatives transform into this new system of coordinates as $\partial_{x_i} = (1/2)\partial_{\overline{x}} + (-1)^{i+1}\partial_{\tilde{x}}$, $\partial_{y_i} = (1/2)\partial_{\overline{y}} + (-1)^{i+1}\partial_{\tilde{y}}$, $\Delta_i = \tilde{\Delta} + (1/4)\overline{\Delta} + (-1)^{i+1}\partial^2_{\tilde{y}\overline{y}} + (-1)^{i+1}\partial^2_{\tilde{x}\overline{x}}$, with $\tilde{\Delta} = \partial^2_{\tilde{x}\tilde{x}} + \partial^2_{\tilde{y}\tilde{y}}$ and $\overline{\Delta} = \partial^2_{\overline{x}\overline{x}} + \partial^2_{\overline{y}\overline{y}}$. It is also convenient to introduce the stream function covariance $S(\tilde{x},\overline{x},\tilde{y},\overline{y}) \equiv \left\langle\psi_1'\psi_2'\right\rangle$, which is related to $C(\tilde{x},\overline{x},\tilde{y},\overline{y})$ via

$$C = \left\langle\zeta_1'\zeta_2'\right\rangle = \left\langle\Delta_1\psi_1'\Delta_2\psi_2'\right\rangle = \Delta_1\Delta_2 S \\ = \left[\left(\tilde{\Delta} + \frac{1}{4}\overline{\Delta}\right)^2 - \Gamma^2\right]S, \tag{27.B.1}$$

where $\Gamma = \partial^2_{\tilde{x}\overline{x}} + \partial^2_{\tilde{y}\overline{y}}$. Equations (27.9) and (27.12) then become, in the absence of hyperviscosity ($\nu = 0$),

$$\left[\partial_t + \overline{U}\partial_{\overline{x}} + \tilde{U}\partial_{\tilde{x}} + \overline{V}\partial_{\overline{y}} + \tilde{V}\partial_{\tilde{y}}\right]C + \\ + \left[(\beta + \overline{Z}_y)\partial_{\overline{x}} + \tilde{Z}_y\partial_{\tilde{x}} - \overline{Z}_x\partial_{\overline{y}} - \tilde{Z}_x\partial_{\tilde{y}}\right]\left(\tilde{\Delta} + \frac{1}{4}\overline{\Delta}\right)S - \\ - \left[2(\beta+\overline{Z}_y)\partial_{\tilde{x}} + \frac{1}{2}\tilde{Z}_y\partial_{\overline{x}} - 2\overline{Z}_x\partial_{\tilde{y}} - \frac{1}{2}\tilde{Z}_x\partial_{\overline{y}}\right]\Gamma S = \\ = -2rC + \Xi, \tag{27.B.2}$$

$$(\partial_t + \mathbf{U}\cdot\nabla)Z + \beta V = (\partial^2_{\tilde{x}\overline{y}} - \partial^2_{\tilde{y}\overline{x}})\Gamma S|_{\tilde{x}=\tilde{y}=0} - rZ, \tag{27.B.3}$$

where $(\overline{U},\overline{V}) = (1/2)(U_1+U_2, V_1+V_2)$, $(\tilde{U},\tilde{V}) = (U_1-U_2, V_1-V_2)$, $(\overline{Z}_x,\overline{Z}_y) = (1/2)(\partial_{x_1}+\partial_{x_2},\partial_{y_1}+\partial_{y_2})Z$ and $(\tilde{Z}_x,\tilde{Z}_y) = (\partial_{x_1}-\partial_{x_2},\partial_{y_1}-\partial_{y_2})Z$.

The forcing covariance Ξ is homogeneous, and as a result it depends only on the difference coordinates, $\tilde{x}$ and $\tilde{y}$. It can then be readily shown from (27.B.2) and (27.B.3) that the state with no coherent flow ($U^\mathrm{E} = V^\mathrm{E} = Z^\mathrm{E} = 0$) and with the homogeneous vorticity covariance $C^\mathrm{E}(\tilde{x},\tilde{y}) = \Xi/(2r)$ (implying also that the stream function covariance S^E is homogeneous) is a fixed point of the S3T system. The stability of this homogeneous equilibrium can be addressed by first linearizing the S3T system about it:

$$\partial_t\delta C = -\left(\delta\tilde{U}\partial_{\tilde{x}} + \delta\tilde{V}\partial_{\tilde{y}}\right)C^\mathrm{E} - \left(\delta\tilde{Z}_y\partial_{\tilde{x}} - \delta\tilde{Z}_x\partial_{\tilde{y}}\right)\tilde{\Delta}S^\mathrm{E} - \\ - \beta\left\{\left[\tilde{\Delta} + \frac{1}{4}\overline{\Delta}\right]\partial_{\overline{x}} - 2\Gamma\partial_{\tilde{x}}\right\}\delta S - 2r\delta C, \tag{27.B.4}$$

$$\partial_t\delta Z = -\beta\delta V + (\partial^2_{\tilde{x}\overline{y}} - \partial^2_{\tilde{y}\overline{x}})\Gamma\delta S|_{\tilde{x}=\tilde{y}=0} - r\delta Z, \tag{27.B.5}$$

where δZ, $\delta\tilde{U}$, $\delta\tilde{V}$, $\delta\tilde{Z}_x$, $\delta\tilde{Z}_y$, δC and δS are small perturbations in the ensemble mean vorticity, velocities and vorticity gradients, and in the eddy vorticity and stream function covariances respectively, and then performing an eigenanalysis of the linearized equations (27.B.4) and (27.B.5).

We consider a harmonic vorticity perturbation of the form $\delta Z = e^{inx+imy}e^{\sigma t}$, for which

$$[\delta\tilde{U},\delta\tilde{V},\delta\tilde{Z}_x,\delta\tilde{Z}_y] = \\ = -2\left[\frac{m}{N^2},-\frac{n}{N^2},n,m\right]\sin\left(\frac{n\tilde{x}}{2}+\frac{m\tilde{y}}{2}\right)e^{in\overline{x}+im\overline{y}}e^{\sigma t}, \tag{27.B.6}$$

with $N^2 = n^2+m^2$. Taking the same form for the stream function covariance perturbation $\delta S = S_{nm}(\tilde{x},\tilde{y})e^{in\overline{x}+im\overline{y}}e^{\sigma t}$ and inserting it in (27.B.4) and (27.B.5) along with (27.B.6) yields

$$(\sigma+2r)\left[\left(\tilde{\Delta} - \frac{N^2}{4}\right)^2 + \Delta_+^2\right]S_{nm} \\ - \left[2i\beta\Delta_+\partial_{\tilde{x}} - in\beta\left(\tilde{\Delta} - \frac{N^2}{4}\right)\right]S_{nm} = \\ = \frac{2}{N^2}\sin\left(\frac{n\tilde{x}}{2}+\frac{m\tilde{y}}{2}\right)\left(m\partial_{\tilde{x}} - n\partial_{\tilde{y}}\right)(\tilde{\Delta}+N^2)\tilde{\Delta}S^\mathrm{E}, \tag{27.B.7}$$

$$-(\sigma+r)N^2 + in\beta = N^2\left(m\partial_{\tilde{x}} - n\partial_{\tilde{y}}\right)\Delta_+ S_{nm}|_{\tilde{x}=\tilde{y}=0}, \tag{27.B.8}$$

where $\Delta_+ = n\partial_{\tilde{x}} + m\partial_{\tilde{y}}$ and $C^\mathrm{E} = \Xi/2r = \tilde{\Delta}^2 S^\mathrm{E}$ is the equilibrium vorticity covariance with zero mean flow.

Defining the Fourier transform of $S_{nm}(\tilde{x},\tilde{y})$ by

$$\hat{S}_{nm}(k,l) = \frac{1}{2\pi}\int_{-\infty}^{\infty}\int_{-\infty}^{\infty} S_{nm}(\tilde{x},\tilde{y})e^{-ik\tilde{x}-il\tilde{y}}\mathrm{d}\tilde{x}\mathrm{d}\tilde{y}, \qquad (27.B.9)$$

we obtain from (27.B.7) that the Fourier component $\hat{S}_{nm}$ satisfies

$$\hat{S}_{nm} = \frac{(mk_- - nl_-)K_-^2(K_-^2/N^2-1)\hat{S}^{\mathrm{E}}(k_-,l_-)}{i\beta(k_-K_+^2 - k_+K_-^2)+(\sigma+2r)K_+^2K_-^2} - \\ - \frac{(mk_+ - nl_+)K_+^2(K_+^2/N^2-1)\hat{S}^{\mathrm{E}}(k_+,l_+)}{i\beta(k_-K_+^2 - k_+K_-^2)+(\sigma+2r)K_+^2K_-^2}, \qquad (27.B.10)$$

with $k_\pm = k \pm n/2$, $l_\pm = l \pm m/2$, $K_\pm^2 = k_\pm^2 + l_\pm^2$ and $K^2 = k^2+l^2$. $\hat{S}^{\mathrm{E}} = \hat{\Xi}/(2rK^4)$ is the Fourier transform of S^{E}, and $\hat{\Xi}$ is the Fourier transform of Ξ. In addition, (27.B.8) becomes

$$in\beta - (\sigma+r)N^2 = \\ = -\frac{N^2}{2\pi}\int_{-\infty}^{\infty}\int_{-\infty}^{\infty}\left[nm(k^2-l^2)+(m^2-n^2)kl\right]\hat{S}_{nm}\mathrm{d}k\mathrm{d}l \\ = \Lambda_+ - \Lambda_-, \qquad (27.B.11)$$

where

$$\Lambda_\pm = \frac{1}{2\pi}\int_{-\infty}^{\infty}\int_{-\infty}^{\infty}\mathrm{d}k\mathrm{d}l K_\pm^2(K_\pm^2 - N^2)\hat{S}^{\mathrm{E}}(k_\pm,l_\pm)\times \\ \times \frac{\left[nm(k^2-l^2)+(m^2-n^2)kl\right](mk_\pm - nl_\pm)}{i\beta(k_-K_+^2 - k_+K_-^2)+(\sigma+2r)K_+^2K_-^2}. \qquad (27.B.12)$$

Equation (27.B.11) can be further simplified by noting that because the choice of $\mathbf{x}_1$ and $\mathbf{x}_2$ is arbitrary, the forcing covariance satisfies the exchange symmetry $\Xi(x_1,x_2,y_1,y_2) = \Xi(x_2,x_1,y_2,y_1)$. In terms of the new variables, the exchange symmetry is written as $\Xi(\tilde{x},\overline{x},\tilde{y},\overline{y}) = \Xi(-\tilde{x},\overline{x},-\tilde{y},\overline{y})$, and consequently $\hat{\Xi}$ satisfies $\hat{\Xi}(-k,-l) = \hat{\Xi}(k,l)$. As a result,

$$\Lambda_+ = -\Lambda_-. \qquad (27.B.13)$$

sign of k in the integral to obtain

$$\int_{-\infty}^{\infty}\int_{-\infty}^{\infty}\mathrm{d}k\mathrm{d}l\ K^2(K^2-N^2)\hat{S}^{\mathrm{E}}(-k,l)\times \\ \times \frac{(mk-nl)\left[nm(k_+^2-l_+^2)+(m^2-n^2)k_+l_+\right]}{-i\beta\left(kK_s^2-(k+n)K^2\right)+(\sigma_{(-n,m)}+2r)K^2K_s^2} = \\ = \pi(\sigma_{(-n,m)}+r)N^2 + i\pi n\beta. \qquad (27.B.16)$$

Using (27.B.13) and shifting the axes in the resulting integrals ($k \to k+n/2$ and $l \to l+m/2$), reduces (27.B.11) to the following dispersion relation:

$$\int_{-\infty}^{\infty}\int_{-\infty}^{\infty}\mathrm{d}k\mathrm{d}l\ K^2(K^2-N^2)\hat{S}^{\mathrm{E}}(k,l)\times \\ \times \frac{(mk-nl)\left[nm(k_+^2-l_+^2)+(m^2-n^2)k_+l_+\right]}{i\beta\left(kK_s^2-(k+n)K^2\right)+(\sigma+2r)K^2K_s^2} = \\ = \pi(\sigma+r)N^2 - i\pi n\beta, \qquad (27.B.14)$$

where $K_s^2 = (k+n)^2+(l+m)^2$. The corresponding dispersion relation on a periodic box can be readily calculated by simply substituting the integrals in (27.B.14) by finite sums of integer wavenumbers. For a mirror symmetric forcing obeying

$$\hat{\Xi}(-k,l) = \hat{\Xi}(k,l), \qquad (27.B.15)$$

the eigenvalues σ satisfy the symmetries (27.17). In order to show this, we consider (27.B.14) for $\sigma_{(-n,m)}$ and change the Taking the conjugate of (27.B.16) and using the mirror symmetry (27.B.15) yields (27.B.14), and therefore $\sigma_{(-n,m)} = \sigma^*_{(n,m)}$. Similarly, it can be readily shown, by considering (27.B.14) for $\sigma_{(n,-m)}$ and changing the sign of l in the integral, that $\sigma_{(n,-m)} = \sigma_{(n,m)}$.